



Research Article

High-resolution lithostratigraphy and organic carbon isotope stratigraphy of the Lower Triassic pelagic sequence in central Japan

HIRONOBU SAKUMA,¹ RYUJI TADA,^{1*} MASAYUKI IKEDA,¹ YUICHIRO KASHIYAMA,²
NAOHIKO OHKOUCHI,³ NANAOKO O. OGAWA,³ SATOKO WATANABE,¹ EIICHI TAJIKA¹ AND
SHINJI YAMAMOTO¹

¹*Department of Earth and Planetary Science, University of Tokyo, 7-3-1 Hongo, Bunkyo-ku, Tokyo 113-0033, Japan (email: ryuji@eps.s.u-tokyo.ac.jp),* ²*Department of Chemistry, University of Tsukuba, 1-1-1 Tennodai, Tsukuba, Ibaraki 305-8571, Japan,* ³*Institute of Biogeosciences, Japan Agency for Marine-Earth Science and Technology, 2-15 Natsushima, Yokosuka, Kanagawa 237-0061, Japan*

Abstract After the severest mass extinction event in the Phanerozoic, biotic recovery from the extinction at the Permian–Triassic boundary required approximately 5 my, which covers the entire Early Triassic. It is important to obtain information on the superocean Panthalassa, which occupied most of the world ocean, to explore paleoenvironmental changes during the Early Triassic at the global scale. In order to establish the continuous lithostratigraphy of pelagic sediments in Panthalassa during the Early Triassic, high-resolution reconstruction of the Lower Triassic pelagic sequence in Japan was conducted for the first time based on detailed field mapping and lithostratigraphic correlation in the Inuyama area, central Japan. The reconstructed Early Triassic sequence is approximately 9.5 m thick, consists of five rock types, and is divided into eight lithological units. For the reconstructed continuous sequence, measurement of carbon isotopic composition of sedimentary organic matter ($\delta^{13}\text{C}_{\text{org}}$) was carried out. Stratigraphic variation of the $\delta^{13}\text{C}_{\text{org}}$ value shows large-amplitude fluctuations between -34.4 and -21.0% throughout the sequence. In order to establish a higher resolution age model for the reconstructed Lower Triassic pelagic sequence, we correlated $\delta^{13}\text{C}_{\text{org}}$ records in the Inuyama area with high-resolution isotopic profiles of carbonate carbon ($\delta^{13}\text{C}_{\text{carb}}$) from shallow-marine carbonate sequences in southern China based on the similarity in general variation patterns with age constraints by radiolarian and conodont biostratigraphy. The result provides a high-resolution time scale for the pelagic sequence of Panthalassa during the Smithian and Spathian. The age model suggests a drastic increase in sedimentation rate during the late Smithian, which should have been caused by the increase in terrigenous input to this site.

Key words: carbon isotope, Lower Triassic, mass extinction, pelagic sequence, Permian–Triassic boundary, siliceous rock.

INTRODUCTION

The Permian–Triassic (P–T) boundary is characterized by the largest mass extinction in the Phanerozoic with global loss of nearly 90% of marine species (Erwin 1994). Besides the magnitude of the extinction, the conspicuous aspect of the P–T

boundary mass extinction event is its aftermath. A delayed biotic recovery after the mass extinction lasted until the end of the Early Triassic, which is characterized by low diversity of marine invertebrate fauna (Schubert & Bottjer 1995) as well as the absence of metazoan reefs (Flügel 2002). Recently, it was demonstrated that continuous carbon cycle instability characterized by large-amplitude carbon isotopic oscillations lasted during the Early Triassic, which was reported

*Correspondence.

Received 28 December 2010; accepted for publication 26 January 2012.

from shallow-marine carbonate sequences deposited in the tropical Tethys (Payne *et al.* 2004; Galfetti *et al.* 2007a), possibly representing the repeated environmental disturbances that inhibited biotic recovery. To explore paleoenvironmental changes during the Early Triassic at the global scale, it is important to obtain information on the superocean Panthalassa, which occupied most of the world ocean, and to compare the result with that obtained from shallow-marine environments.

The Jurassic accretionary complex in Japan contains a Permian–Triassic pelagic sedimentary sequence deposited on the deep seafloor of Panthalassa, which is considered to have recorded global environmental changes (Isozaki 1997). Lithostratigraphic and biostratigraphic studies on the sequence across the P–T boundary have been conducted in several regions in Japan (Fig. 1), and the schematic composite column, which consists of Upper Permian chert, uppermost Permian siliceous claystone, uppermost Permian to lowermost Triassic black shale, Lower Triassic siliceous claystone, and Middle Triassic chert in ascending order was constructed (e.g. Yamakita 1993; Isozaki 1997). The earliest Triassic conodont, *Hindeodus parvus*, was reported from a thin gray siliceous claystone bed that is intercalated approximately 10 cm above the base of black shale at Ubara section in Southwest Japan (Yamakita *et al.* 1999) and 80 cm above the base of black shale at Akkamori section in Northeast Japan (Takahashi *et al.* 2009a), implying that the P–T boundary is placed

near the base of the black shale. The absence of radiolarian bedded chert for several million years across the P–T boundary is widely recognized in the pelagic sequence of Japan and is considered to have been related to anoxic conditions in the deep ocean (e.g. Kajiwarara *et al.* 1994; Isozaki 1997; Kato *et al.* 2002; Kakuwa 2008; Algeo *et al.* 2010; Wignall *et al.* 2010).

The lithostratigraphic sequence across the P–T boundary in Japan has been reconstructed based on the schematic compilation of fragmental and discontinuous lithological sequences from several different localities, because the pelagic sequences were intensely faulted and folded during the accretionary process and especially the black shale became the slip horizon (e.g. Nakae 1993). Consequently, the continuous uppermost Permian and Lower Triassic lithostratigraphic succession and its detailed chronology from the lowermost Triassic black shale up to the lowermost Middle Triassic bedded chert are still unknown.

Here, we carried out detailed field mapping of the Jurassic accretionary complex of Mino Belt exposed at Momotaro Shrine section along the Kiso River, Inuyama area, central Japan, and reconstructed an approximately 9.5 m-thick continuous composite sedimentary sequence of the Early Triassic based on correlation and stacking of columnar sections made for individual fault-bounded blocks. Detailed description of the Early Triassic lithostratigraphy, organic carbon isotope stratigraphy, and its correlation with carbonate

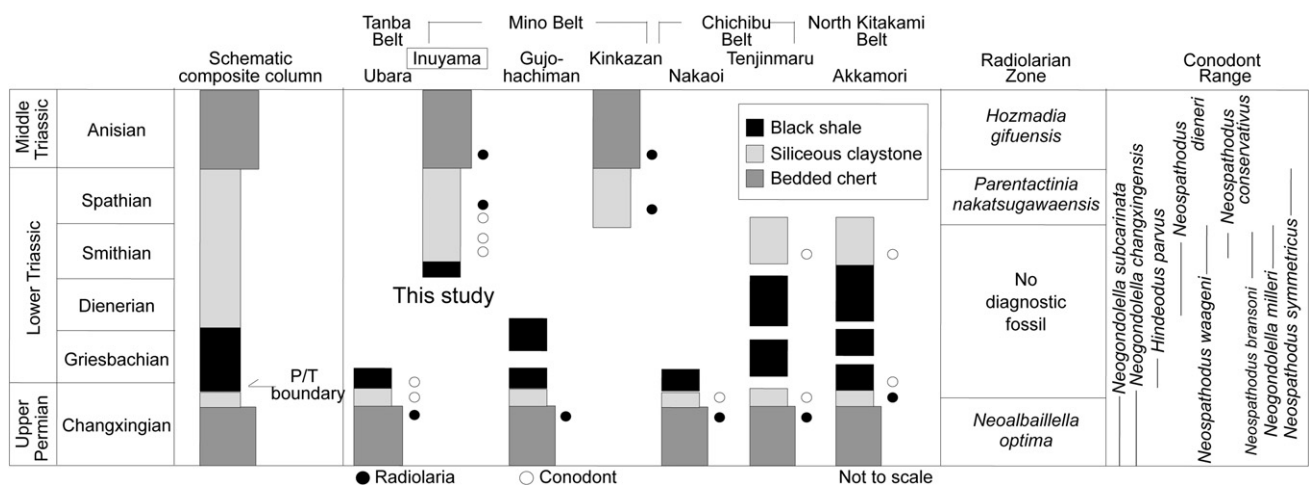


Fig. 1 Schematic composite column of the pelagic sequence from the Late Permian to Middle Triassic in Japan (Isozaki 1997) and fragmental sequences in Ubara (Kuwahara *et al.* 1991; Yamakita *et al.* 1999), Kinkazan (Sugiyama 1992), Gujo-hachiman (Kuwahara *et al.* 1991), Inuyama (Yao & Kuwahara 1997; this study), Nakaio (Yamakita 1993; Kuwahara & Yamakita 2001), Tenjinmaru (Yamakita 1987; Kuwahara & Yamakita 2001), and Akkamori (Takahashi *et al.* 2009a) in southwest to northeastern Japan with radiolarian zone (Sugiyama 1992; Yao & Kuwahara 1997; Kuwahara & Yamakita 2001) and conodont range (Yamakita 1993; Orchard 1995, 2007). The schematic column was inferred from lithological and fossil information from fragmental sequences as shown above.

carbon isotope stratigraphy established in the shallow-water environment in the Tethys is presented in this study.

GEOLOGICAL SETTING

The studied section is located in the Inuyama area, Mino Belt, central Japan. The Jurassic accretionary complex, which includes the Mino Belt and mainly consists of the Middle Triassic-Lower Jurassic bedded chert unit and the Middle–Upper Jurassic clastic rock unit, is well exposed along the Kiso River in the Inuyama area (Matsuda & Isozaki 1991). The lowermost part of the bedded chert unit in the Inuyama area mainly consists of black shale and gray siliceous claystone, which are associated with dolostone nodules and nodular beds (Yao & Kuwahara 1997; Tada *et al.* 2005). This stratigraphic interval corresponds to the Lower Triassic and is the focus of this study. Paleomagnetic studies on red bedded chert from The Inuyama area suggest a paleolatitude of $0.7 \pm 3.4^\circ$ for the Middle Triassic (Shibuya & Sasajima 1986), $12.3 \pm 15.6^\circ$, $19.0 \pm 10.5^\circ$, and $25.7 \pm 16.7^\circ$ for the Middle–Upper Triassic (Oda & Suzuki 2000), and $11.0 \pm 4.3^\circ$ for the Middle Triassic – Lower Jurassic (Ando *et al.* 2001), suggesting that the Triassic–Jurassic pelagic sequence in the Inuyama area was deposited at low latitude, presumably near the equator. The lithostratigraphic transition from the Lower Jurassic bedded chert to the Middle to

Upper Jurassic clastic rock is interpreted as reflecting changes in the depositional setting from the deep sea floor to the trench in the subduction zone (Matsuda & Isozaki 1991; Kimura & Hori 1993). Previous radiolarian and conodont biostratigraphy revealed that average sedimentation rates of the Middle Triassic–Lower Jurassic bedded chert in the Inuyama area range from 1 to 4 mm/ky (e.g. Yao *et al.* 1980; Yao 1982; Matsuda & Isozaki 1991), which is consistent with the interpretation that bedded chert in the Inuyama area was deposited in an open ocean setting remote from continents so that the site was prevented from abundant terrigenous influx for at least 50 my (Matsuda & Isozaki 1991).

METHODS AND MATERIALS

FIELD MEASUREMENT

The studied outcrop, around 50 m × 50 m in area, is located near the Momotaro Shrine on the east side of the Kiso River in Inuyama City (Fig. 2). The outcrop provides a widespread exposure of the Lower Triassic sedimentary sequence in the lowermost part of the bedded chert unit (= unit CH-3 of Yao *et al.* 1980). The outcrop includes Section MT of Yao and Kuwahara (1997), Section T of Sugiyama (1997), Section Momotaro Shrine of Tada *et al.* (2005), and Section Mj of Takahashi *et al.* (2009b). However, detailed field mapping,

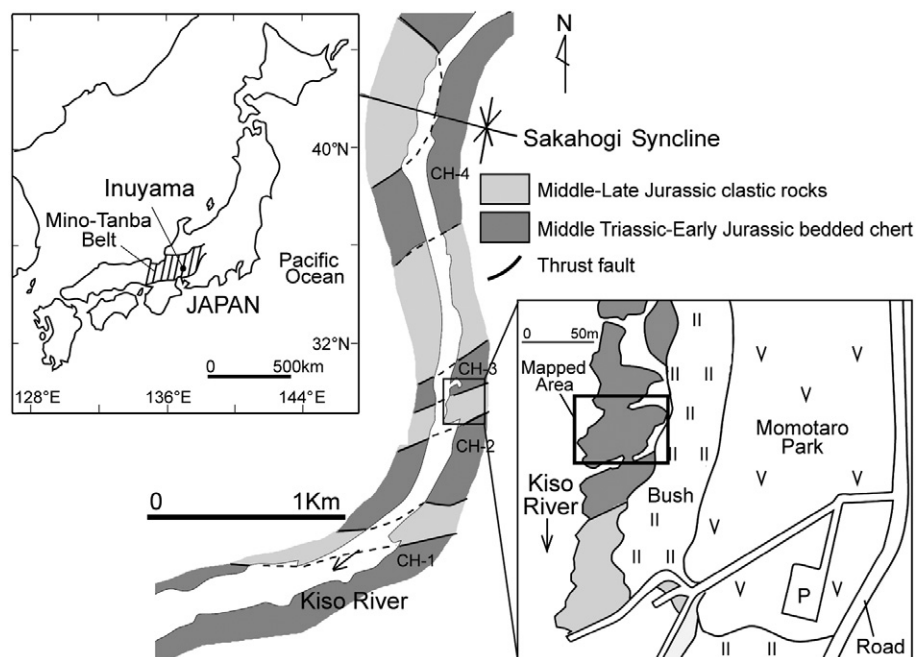


Fig. 2 Maps showing the location of Inuyama city, general geological setting around the Inuyama area, and the location of mapped area. Bedded chert units CH-1 to -4 divided by thrust faults are after Yao *et al.* (1980). The mapped area is located on the thrust sheet of bedded chert unit CH-3.

description of the whole outcrop, and continuous lithostratigraphic reconstruction have never been conducted. In this study, detailed field mapping was carried out in an area near the Momotaro Shrine to reconstruct the Lower Triassic pelagic sequence.

CARBON ISOTOPIC ANALYSIS

One hundred and eight samples, each generally representing stratigraphic intervals of 3–10 cm, were sampled from the reconstructed sequence exposed on the studied outcrop with an average spacing of 4 cm. After removal of the weathered surface, each sample was pulverized in a tungsten mortar, and then treated with HCl to remove carbonates.

Measurements of total organic carbon (TOC) contents and isotopic compositions of TOC ($\delta^{13}\text{C}_{\text{org}}$) of these samples were performed using an on-line system of isotope-ratio mass spectrometry (Delta Plus XP; Finnigan, Waltham, MA, USA) coupled to a Flash EA 1112 Automatic Elemental Analyzer through a ConFlo III interface at the Japan Agency for Marine-Earth Science and Technology (e.g. Ohkouchi *et al.* 2005). The carbon isotopic compositions are expressed in delta (δ) notation against the Vienna Pee Dee belemnite standard (VPDB) with analytical errors (1σ) better than 0.2‰ based on repeated measurements of authenticated and laboratory standards.

RESULT

MOMOTARO SHRINE SECTION IN INUYAMA AREA

Field mapping

Faults

Faults are classified into four types based on their dip and strike trends. Type I is characterized by a strike of around N80°E and has an almost vertical dip with fault gouge 1–3 cm in thickness. Type II is characterized by a strike of N65° to 70°E and dip of 70°N. Type III is characterized by a strike of N80°E to east–west and an almost vertical dip. Type IV is characterized by a strike of N30° to 40°E and dip of 60°E. There is no distinct fault gouge associated with Type II, III, and IV faults. Type I faults are major faults that divide the studied outcrop into northern and southern blocks (Fig. 3), and bounds the southern limit of the

studied area. Type II faults occur only in the northern block. Type III faults occur in the northern block and in the southern part of southern block. Type IV faults occur only in the southern block. Hence, most faults in the studied area occur in the northern block and the southern part of southern block, whereas only a few minor faults occur in the northern part of southern block.

The accurate strike separation of Type I faults is unknown, but it could be more than several meters based on lithological correlation between the both sides of the faults. They are considered as subordinate faults associated with formation of the thrust sheet of bedded chert unit CH-3, judging from their dip and strike trends, which are similar to those of the thrust faults. Strike separations of Type II, III, and IV faults are estimated to be tens of centimeters to several meters according to our field observations. Type I faults cut Type II and III faults, and Type II faults cut Type III faults in the northern block. In addition, Type III faults cut Type IV faults in the southern block. Judging from the cross-cutting relationships between these faults, the chronological order of their formation is estimated as Types IV, III, II, and I in younging order. Type IV, III, and II faults are considered to have been formed in association with the folding process preceding the formation of thrust sheets.

Folds

All folds in the studied area have fold axis directions approximately east–west and plunge westward by around 30°. However, there is a slight difference in dips and strikes of their axial surfaces: folds with dips and strikes of approximately 70°N and N80°E occur in the northern block, and approximately 60° to 80°S and east–west to N80°W occur in the southern block. This may reflect slight rotational movement between northern and southern blocks, which are bounded by the Type I fault. Wavelengths and interlimb angles of folds are different depending on the lithologies. Namely, wavelength is 1 to 5 m and interlimb angle is around 40° in argillaceous chert, whereas they are less than 1 m and 10° to 30° in siliceous mudstone, probably reflecting differences in physical property of each lithology.

The studied area is located in the south wing of the Sakahogi Syncline (Fig. 2) that plunges to the west by around 78° with the east–west syncline axis direction (Kimura & Hori 1993). Folds in the studied area are considered to have been formed at the same stage as formation of the Sakahogi

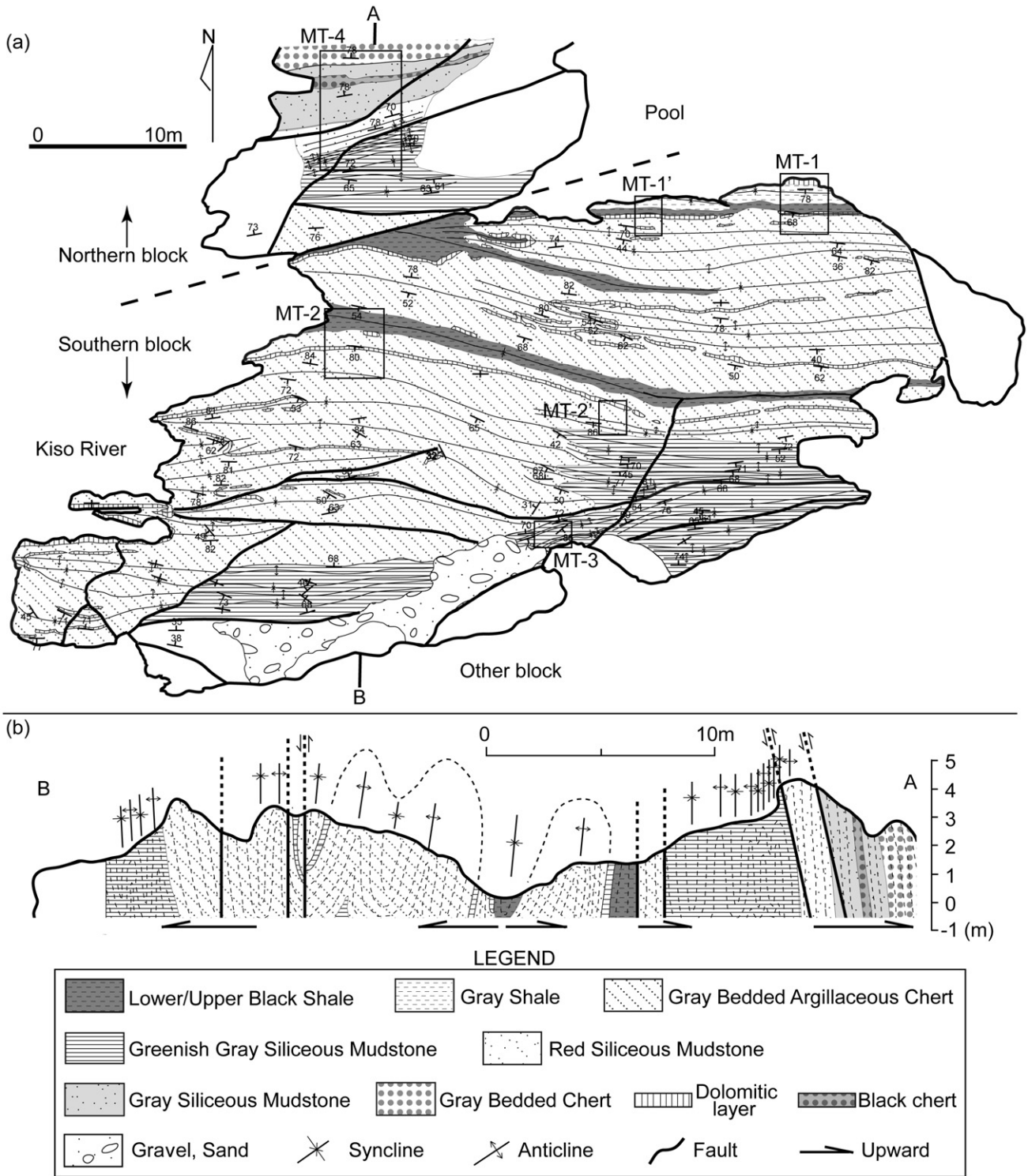


Fig. 3 (a) Geologic sketch map with locations of the six sections (rectangles) (MT-1, -1', -2, -2', -3, and -4), and (b) cross-sectional profile of the mapped area near Momotaro Shrine.

Syncline during the accretionary process by north-south compression (Kimura & Hori 1993), judging from the similar fold axis directions between these folds. The folds in the studied area

are cut by a Type II fault in the northern block and a Type IV fault in the southern part of southern block, suggesting that they have been formed earlier than these faults.

Establishment of high-resolution continuous lithostratigraphy

Five rock types were recognized in the studied outcrop as follows.

Shale

Shale is either massive or laminated. It shows two varieties in color: gray and black. Gray shale occurs as a 10–30 cm-thick bed or a thin bed of less than 2 cm thick, and the latter alternates with siliceous mudstone, argillaceous chert, and chert. Black shale occurs as a 0.5–100 cm-thick bed, which is partly sheared and shows planar partings parallel to the bedding on the weathered surface. Black shale also occurs as a thin bed of less than 3 cm thick that alternates with siliceous mudstone and argillaceous chert.

Siliceous mudstone

It occurs as a 5–30 cm-thick bed, and shows three color varieties: greenish gray, gray, and red. Greenish gray siliceous mudstone is either massive or laminated, often alternates with a black shale bed 0.5 to 3 cm thick, and shows yellowish color on the weathered surface. Gray and red siliceous mudstone is 5 to 20 cm thick, dominantly massive or slightly laminated, and often alternates with a chert bed 1 to 3 cm thick. Gray siliceous mudstone also alternates with a gray shale bed <2 cm thick.

Argillaceous chert

Argillaceous chert occurs as a 5–15 cm-thick bed, which is either massive or laminated, and gray to dark gray in color. It generally alternates with a gray shale bed of less than 2 cm thick, and often alternates with a black shale bed of 0.5 to 3 cm thick.

Chert

It is dominantly massive or slightly laminated. It shows three color varieties: gray, black, and red. Gray chert occurs as an approximately 5 cm-thick bed that alternates with a gray shale bed of less than 2 cm thick, or as a thin bed of 1 to 2 cm thick that is intercalated in gray shale or alternates with gray siliceous mudstone. Black chert occurs as an approximately 15 cm-thick bed that is intercalated in gray siliceous mudstone. Red chert occurs as a

0.5–3 cm-thick bed, which alternates with a red siliceous mudstone.

Dolomitic layer

Dolomitic layer represents mat luster and slightly yellowish gray to light gray in color. It occurs either as a 10–30 cm-thick bed or a nodule of as large as 25 cm in diameter, which is either massive or laminated.

On the basis of rock types and their combination, eight lithological units were identified at the outcrop (Figs 3,4). The lithology of each section is described sequentially on the basis of rock types and their associations, which then is used to identify lithological units and establish continuous lithostratigraphy. Reconstruction of the lithostratigraphic sequence was based on correlation and stacking of six columnar sections (MT-1, -1', -2, -2', -3, and -4) that were constructed for individual fault-bounded blocks. Age diagnostic fossils have been found from sections MT-2 and -4, but the stratigraphic direction can be determined by age diagnostic fossils only in section MT-4. Therefore, we start the description from section MT-4, and then correlate and describe other sections in stratigraphically descending order.

Section MT-4

Section MT-4 is located in the northern block (Fig. 3). This section consists of an approximately 4 m-thick continuous sequence of greenish gray siliceous mudstone, red siliceous mudstone, gray siliceous mudstone, and gray chert intervals in ascending order (Fig. 5).

The greenish gray siliceous mudstone interval is composed of 10–30 cm-thick greenish gray siliceous mudstone beds which alternate with 1–3 cm-thick black shale beds and approximately 1 cm-thick gray chert beds. We define this lithological interval as the Greenish Gray Siliceous Mudstone Unit. The late Early Triassic (Spathian) conodont *Neospathodus symmetricus* was reported from greenish gray siliceous mudstone beds of this unit (Takahashi *et al.* 2009b). The lower boundary of the Greenish Gray Siliceous Mudstone Unit in this section is bounded by a fold and the base of this unit is not exposed in this section. The thickness of the exposed part of this unit is 40 cm. Greenish gray siliceous mudstone at the top of this unit changes upward into red siliceous mudstone of the overlying unit with a gradational contact.

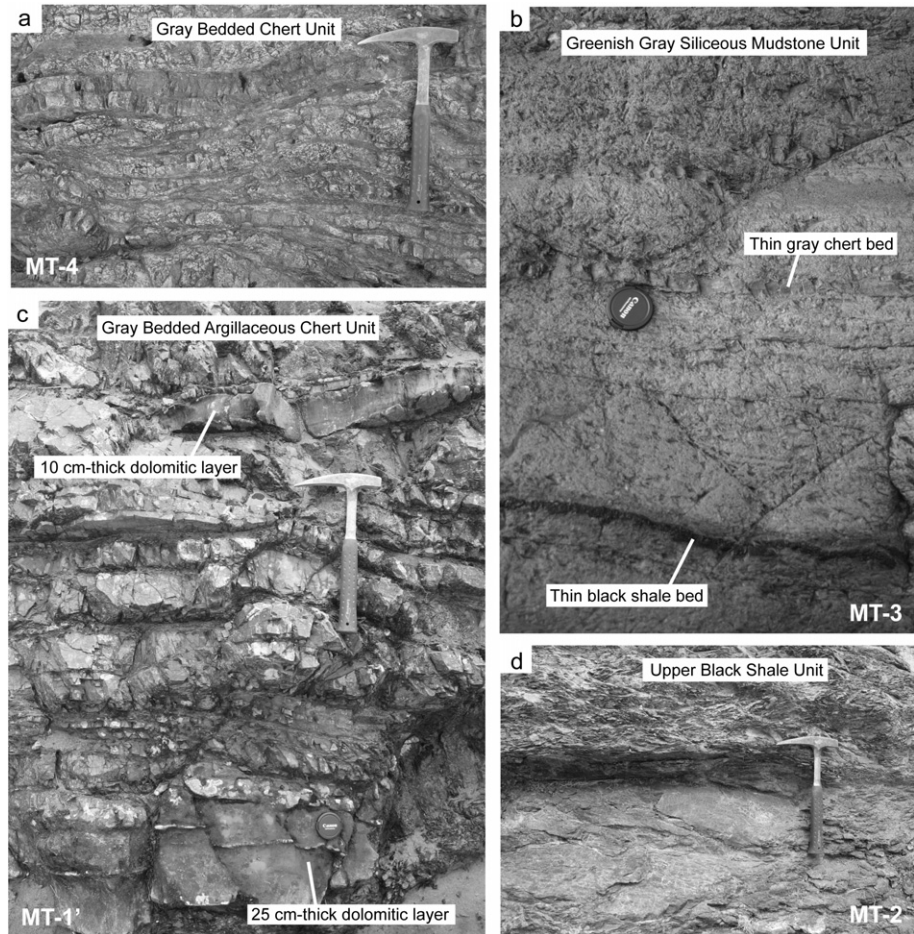


Fig. 4 Photographs of lithological units at the outcrop of Inuyama section. (a) Gray Bedded Chert Unit at section MT-4. (b) Greenish Gray Siliceous Mudstone Unit at section MT-3. (c) Gray Bedded Argillaceous Chert Unit at section MT-1'. (d) Upper Black Shale Unit at section MT-2. See Figure 3 for the locations of sections.

The red siliceous mudstone interval is composed of 5–20 cm-thick red siliceous mudstone beds which alternate with 0.5–3 cm-thick red chert beds. We define this lithological interval as the Red Siliceous Mudstone Unit. The late Early Triassic (Spathian) radiolarian assemblage corresponding to *Parentactinia nakatsugawaensis* zone was reported from a red chert bed of this unit (Yao & Kuwahara 1997). The Red Siliceous Mudstone Unit is approximately 90 cm thick, and changes upward into gray siliceous mudstone of the overlying unit with a gradual contact.

The gray siliceous mudstone interval is composed of 5–15 cm-thick gray siliceous mudstone beds which alternate with less than 1 cm-thick gray shale beds and 2–4 cm-thick gray chert beds. We define this lithological interval as the Gray Bedded Siliceous Mudstone Unit. The Gray Bedded Siliceous Mudstone Unit has an approximately 15 cm-thick intercalation of a black chert bed in its middle part. A radiolarian assemblage corresponding to the *Parentactinia nakatsugawaensis* zone was also reported from a gray chert bed of this unit (Yao & Kuwahara 1997). The Gray

Bedded Siliceous Mudstone Unit is approximately 210 cm thick, and changes upward into gray chert of the overlying unit with a sharp contact.

The gray chert interval is composed of 2–7 cm-thick gray chert beds which alternate with <1 cm-thick gray shale beds. We define this lithological interval as the Gray Bedded Chert Unit. The early Middle Triassic (Anisian) radiolarian assemblage corresponding to the *Hozmadia gifuensis* zone was reported from a gray chert bed of this unit (Yao & Kuwahara 1997). The upper boundary of the Gray Bedded Chert Unit is bounded by a fault and not exposed in this section. The thickness of the exposed part of this unit is 60 cm.

Section MT-3

Section MT-3 is located near the southern limit of the southern block (Fig. 3). This section consists of an approximately 1.5 m-thick continuous sequence of gray argillaceous chert interval and greenish gray siliceous mudstone interval in ascending order (Fig. 5).

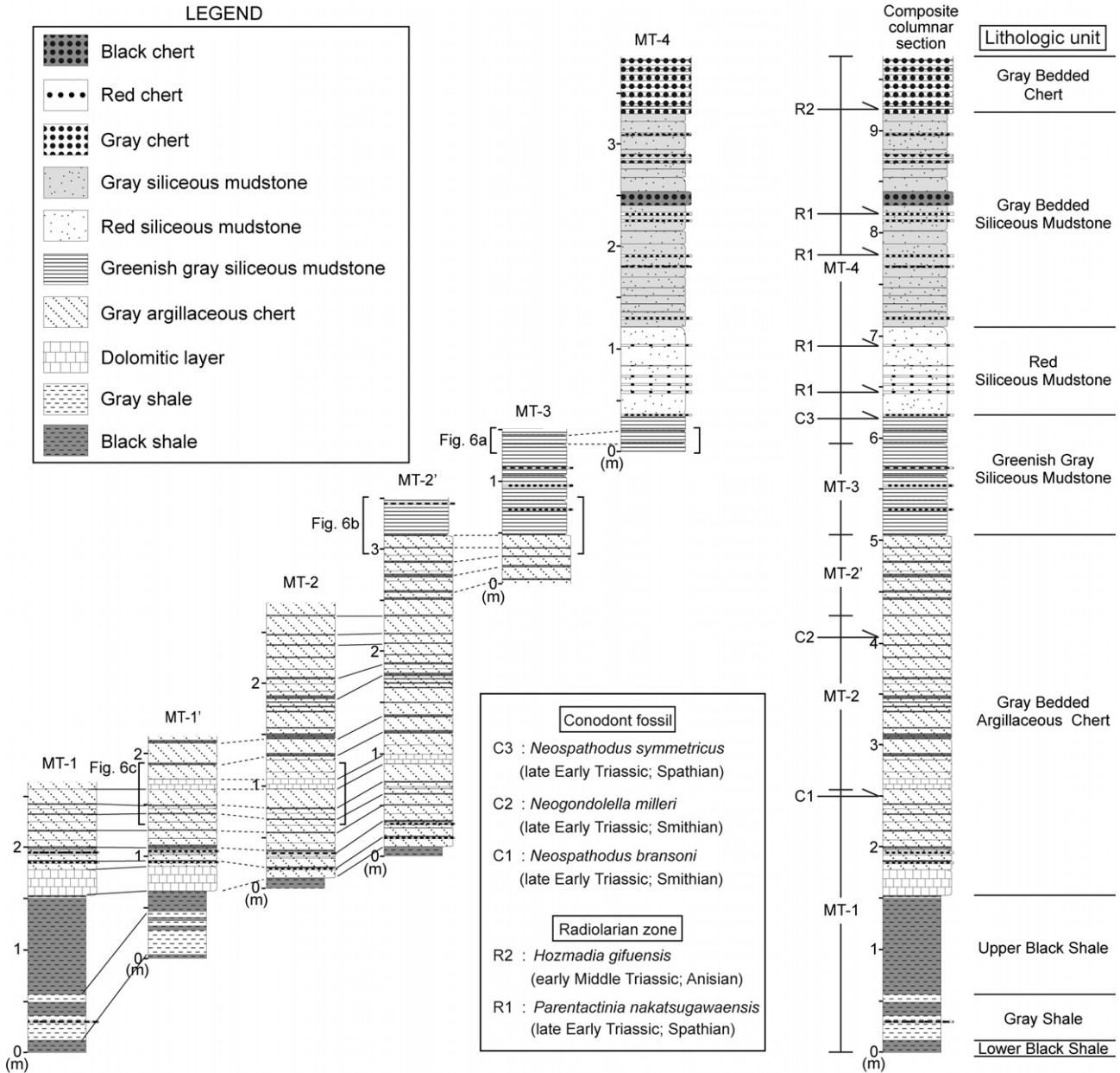


Fig. 5 Correlation of columnar sections at Inuyama section. Solid and dotted lines that correlate columnar sections represent direct and indirect lithostratigraphic correlations, respectively. Arrows indicate horizons that age diagnostic conodont fossils and radiolarian zones have been reported (Yao & Kuwahara 1997; Takahashi *et al.* 2009b; Yamakita *et al.* 2010). Lithostratigraphically correlated intervals at Inuyama section shown in Figure 6 are also indicated on the left or right side of the column. The continuous composite columnar section is shown to the right of the figure.

The gray argillaceous chert interval is composed of 5–15 cm-thick gray argillaceous chert beds which alternate with <1 cm-thick gray shale beds and 1–2 cm-thick black shale beds. We define this lithological interval as the Gray Bedded Argillaceous Chert Unit. The lower limit of the Gray Bedded Argillaceous Chert Unit is bounded by a fault and not exposed in this section. The thickness of the exposed part of this unit is 45 cm. Gray bedded argillaceous chert of this unit changes into greenish gray siliceous mudstone of the overlying

unit with a gradual contact. This boundary can be clearly identified because the spacing between thin black shale beds drastically changes from approximately 10 cm in the gray bedded argillaceous chert interval to 30 cm in the greenish gray siliceous mudstone interval.

The greenish gray siliceous mudstone interval is composed of 10–30 cm-thick greenish gray siliceous mudstone beds which alternate with 0.5–2 cm-thick black shale beds and 0.5–1.5 cm-thick gray chert beds. The appearance of the greenish

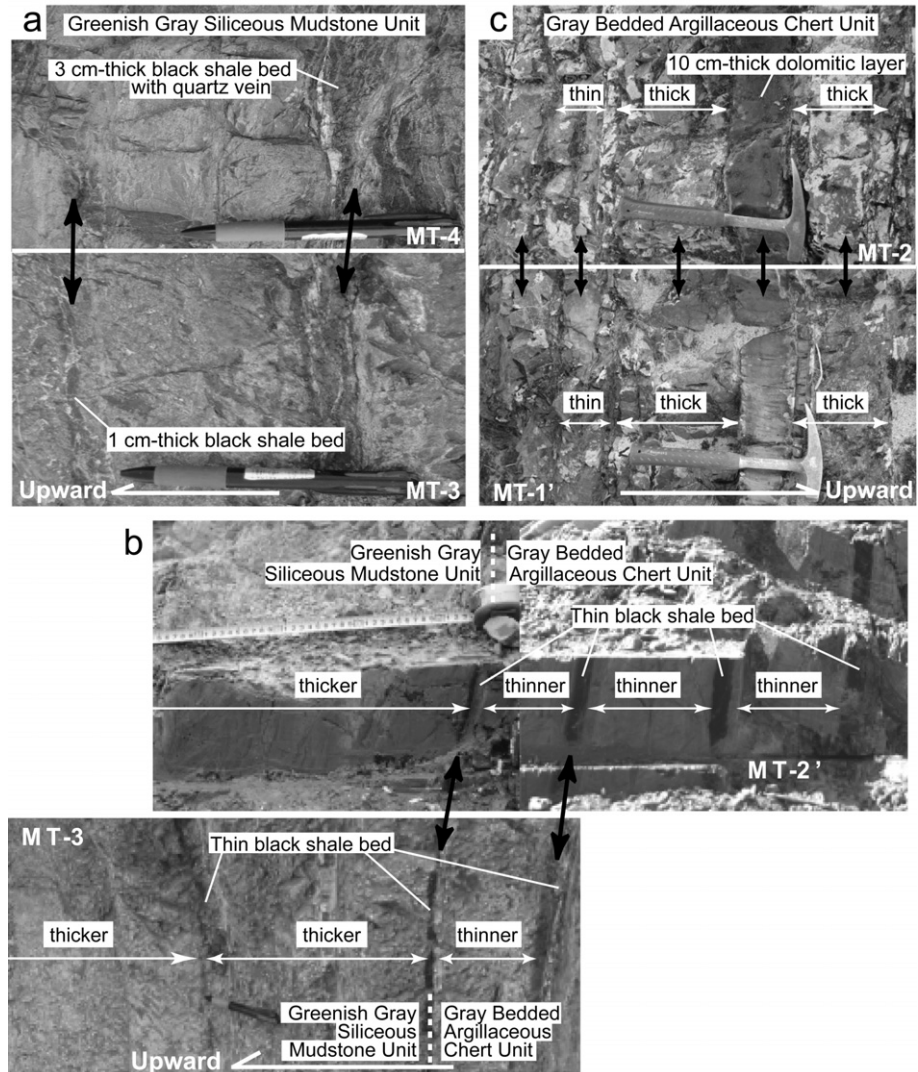


Fig. 6 Photographs showing lithostratigraphic correlations, whose stratigraphic positions are indicated in Figure 5. Correlated beds are tied with double sided black arrows. (a) Correlation of approximately 3 cm-thick black shale bed with quartz vein and 1 cm-thick black shale bed in the Greenish Gray Siliceous Mudstone Unit between sections MT-4 and -3. (b) Correlation of intervals where thin black shale bed are thinner (approximately 10 cm) in the Gray Bedded Argillaceous Chert Unit between sections MT-3 and -2'. (c) Correlation of approximately 10 cm-thick dolomitic layers between sections MT-2 and -1'. Variation patterns in thickness of gray argillaceous chert beds are also correlatable.

gray siliceous mudstone interval is similar to and alternation pattern is correlatable with the Greenish Gray Siliceous Mudstone Unit in section MT-4 (Fig. 6). Especially useful for correlation is an approximately 2 cm-thick black shale bed with white quartz veins, which is used as a marker bed (Fig. 6). Identification of this marker bed allowed us to correlate this interval with the Greenish Gray Siliceous Mudstone Unit. The upper limit of the Greenish Gray Siliceous Mudstone Unit is bounded by a fold and not exposed in this section. The thickness of the exposed part of this unit is 105 cm. Based on the correlation of the Greenish Gray Siliceous Mudstone Unit between this section and section MT-4 using the 2 cm-thick black shale bed with white quartz veins, the thickness of the Greenish Gray Siliceous Mudstone Unit is estimated as 110 to 120 cm. Based on the correlation with section MT-4, this section is composed of the Gray Bedded Argillaceous Chert Unit and

the Greenish Gray Siliceous Mudstone Unit in ascending order.

Section MT-2'

Section MT-2' is located in the southern block (Fig. 3). This section consists of an approximately 3.5 m-thick continuous sequence that is composed of black shale, gray argillaceous chert, dolomitic layer, and greenish gray siliceous mudstone intervals in ascending order (Fig. 5).

The black shale interval is composed of an approximately 105 cm-thick black shale bed which is partly sheared and shows planar partings parallel to the bedding on the weathered surface. We define this lithological interval as the Upper Black Shale Unit. The lower limit of the Upper Black Shale Unit is bounded by a fault and not exposed in this section. Black shale of this unit changes into

gray argillaceous chert of the overlying unit with a sharp contact.

The gray argillaceous chert interval is composed of 5–15 cm-thick gray argillaceous chert beds which alternate with less than 1 cm-thick gray shale beds and 1–2 cm-thick black shale beds. We correlate this lithological interval with the Gray Bedded Argillaceous Chert Unit observed in section MT-3 based on similarity in appearance and alternation pattern. The Gray Bedded Argillaceous Chert Unit intercalates an approximately 10 cm-thick dolomitic layer, which is homogeneous with mat luster, in its lower part. The Gray Bedded Argillaceous Chert Unit is approximately 300 cm thick, and changes into greenish gray siliceous mudstone of the overlying unit with a gradual contact. This boundary can be correlated with that in section MT-3 based on the distinct change in spacing between thin black shale beds, which is approximately 10 cm in the gray bedded argillaceous chert interval and at least 30 cm in the greenish gray siliceous mudstone interval, the latter being similar to the spacings observed in the Greenish Gray Siliceous Mudstone Unit in section MT-3 (Fig. 6).

The greenish gray siliceous mudstone interval in this section is composed of approximately 35 cm-thick greenish gray siliceous mudstone beds which alternate with 0.5 cm-thick black shale beds and 0.5–1.5 cm-thick gray chert beds. We correlate this lithological interval with the Greenish Gray Siliceous Mudstone Unit observed in sections MT-4 and -3 based on similarity in appearance and alternation pattern. The upper limit of the Greenish Gray Siliceous Mudstone Unit is bounded by a fold and not exposed in this section. The thickness of the exposed part of this unit is 35 cm.

Based on correlation with sections MT-4 and -3, this section is composed of the Upper Black Shale Unit, the Gray Bedded Argillaceous Chert Unit, and the Greenish Gray Siliceous Mudstone Unit, in ascending order.

Section MT-2

Section MT-2 is located in the southern block (Fig. 3). This section consists of an approximately 2.8 m-thick continuous sequence of black shale, gray argillaceous chert, and dolomitic layer intervals in ascending order (Fig. 5), which are laterally traceable bed by bed to those in section MT-2'. According to direct tracing of the strata from section MT-2', this section is composed of the Upper Black Shale Unit and the Gray Bedded Argillaceous Chert Unit in ascending order. The lower

limit of the Upper Black Shale Unit is bounded by a fault and not exposed in this section. The thickness of the exposed part of this unit is 10 cm. Black shale of this unit changes into gray argillaceous chert of the overlying Gray Bedded Argillaceous Chert Unit with a sharp contact. Recently, Yamakita *et al.* (2010) reported the late Early Triassic (Smithian) conodonts *Neogondolella milleri* and *Neospathodus bransonii* from the Gray Bedded Argillaceous Chert Unit in this section. The upper limit of the Gray Bedded Argillaceous Chert Unit is bounded by a fold and not exposed in this section. The thickness of the exposed part of this unit is 270 cm.

Section MT-1'

Section MT-1' is located near the northern limit of the southern block (Fig. 3). This section consists of an approximately 2.2 m-thick continuous sequence of black shale, gray shale, black shale, dolomitic layer, and gray argillaceous chert intervals in ascending order (Fig. 5).

The first black shale interval, which is composed of an at least 5 cm-thick black shale bed, is partly sheared and shows planar partings parallel to the bedding on the weathered surface. We define this black shale bed as the Lower Black Shale Unit based on its stratigraphic position. The lower limit of the Lower Black Shale Unit is bounded by a fold and not exposed in this section.

The Lower Black Shale Unit is overlain by an approximately 40 cm-thick interval characterized by alternations of a 5–25 cm-thick gray shale bed and a 1–4 cm-thick black shale bed whose contacts are gradual. We define this lithological interval as the Gray Shale Unit.

The second black shale interval, which is composed of an approximately 20 cm-thick black shale bed with planar partings parallel to the bedding on the weathered surface, occurs above the Gray Shale Unit. We correlate this black shale bed with the Upper Black Shale Unit observed in sections MT-2' and -2 based on the similarity in appearance.

The Upper Black Shale Unit changes into an overlying dolomitic layer with a sharp contact in this section. This dolomitic layer is approximately 25 cm thick, with mat luster, mostly laminated, and intercalated with an approximately 1 cm-thick gray chert bed in its middle part. It is possible to distinguish this dolomitic layer from that in the Gray Bedded Argillaceous Chert Unit in sections MT-2' and -2, because the dolomitic layer in sections MT-2' and -2 is approximately 10 cm thick and dominantly massive. This dolomitic layer

changes upward into gray argillaceous chert with a sharp contact, and belongs to the Gray Bedded Argillaceous Chert Unit.

The gray argillaceous chert interval in section MT-1' is composed of 5–20 cm-thick gray argillaceous chert beds which alternate with less than 1 cm-thick gray shale beds and 1–3 cm-thick black shale beds. We correlate this lithological interval with the Gray Bedded Argillaceous Chert Unit observed in sections MT-3, -2', and -2 based on the similarity in appearance and alternation pattern. The Gray Bedded Argillaceous Chert Unit is intercalated with an approximately 10 cm thick massive dolomitic layer with mat luster in its middle part. We correlate this dolomitic layer with that in the Gray Bedded Argillaceous Chert Unit in sections MT-2' and -2 based on the similarities in thickness, appearance and its stratigraphic position (Fig. 6). The upper limit of the Gray Bedded Argillaceous Chert Unit is bounded by a fold and not exposed in this section. The thickness of the exposed part of this unit is 125 cm. Based on the correlation with sections MT-3, -2', and -2, this section is composed of the Lower Black Shale Unit, the Gray Shale Unit, the Upper Black Shale Unit, and the Gray Bedded Argillaceous Chert Unit, in ascending order.

Section MT-1

Section MT-1 is also located near the northern limit of the southern block (Fig. 3). This section consists of an approximately 2.6 m-thick continuous sequence of black shale, gray shale, black shale, dolomitic layer, and gray argillaceous chert intervals, in ascending order (Fig. 5), which are laterally traceable to section MT-1' bed by bed. Therefore, this section comprises the Lower Black Shale Unit, the Gray Shale Unit, the Upper Black Shale Unit, and the Gray Bedded Argillaceous Chert Unit, in ascending order, based on the direct tracing from those in section MT-1'. The lower limit of the Lower Black Shale Unit is bounded by a fold and not exposed in this section. The thickness of the exposed part of this unit is 10 cm. Black shale of this unit changes into gray shale of the overlying Gray Shale Unit with a gradual contact. The Gray Shale Unit in this section is approximately 45 cm thick, consisting of alternations of a 10–20 cm-thick gray shale bed, a 15 cm-thick black shale bed, and a 1.5 cm-thick gray chert bed, in ascending order. Gray shale of this unit changes into black shale of the overlying Upper Black Shale Unit with a gradational contact. The Upper

Black Shale Unit in this section is approximately 95 cm thick, and changes into an overlying dolomite bed with a sharp contact. The dolomitic layer in this section is approximately 25 cm thick, and changes into gray argillaceous chert with a sharp contact. The upper limit of the Gray Bedded Argillaceous Chert Unit is bounded by a fold and not exposed in this section. The thickness of the exposed part of this unit is 85 cm.

Continuous composite columnar section

Sections MT-4 to MT-1 were correlated with each other, and the continuous composite columnar section covering the entire Lower Triassic was reconstructed (Fig. 5). The composite section is an approximately 9.5 m-thick continuous sequence consisting of the Lower Black Shale Unit, the Gray Shale Unit, the Upper Black Shale Unit, the Gray Bedded Argillaceous Chert Unit, the Greenish Gray Siliceous Mudstone Unit, the Red Siliceous Mudstone Unit, the Gray Bedded Siliceous Mudstone Unit, and the Gray Bedded Chert Unit, in ascending order. The stratigraphic level of 0 cm is set at the exposed lower limit of the Lower Black Shale Unit. Yamakita *et al.* (2010) claimed that the interval examined by this study is overturned on the basis of the occurrence range of two Smithian conodonts *Neogondolella milleri* and *Neospathodus bransoni* after Orchard (2007) in section MT-2. However, these conodonts were originally reported from the same limestone bed approximately 4.5 m thick, which is accompanied with the Smithian ammonoid *Meekoceras* (Müller 1956), suggesting that occurrence ranges of these two conodonts can be overlapped within the Smithian. Therefore, occurrence of these two Smithian conodonts can not be used to determine the stratigraphic direction. In addition, the stratigraphic direction can be estimated based on the nature of the contacts of thin black shale beds, whose basal contact is generally sharp and straight, and the upper contact is gradual (Fig. 7a). Sharp lower contact corresponds to the boundary of depositional environment from oxygen-rich to oxygen-deficient, representing the cessation of bioturbation. On the other hand, gradual upper contact corresponds to the boundary of depositional environment from oxygen-deficient to oxygen-rich, representing the restart of bioturbation. Moreover, burrows filled with black shales are observed in the adjacent Gray Shale Unit (Fig. 7b), suggesting the boring directions of benthos is consistent with our interpretation of the stratigraphic direction.

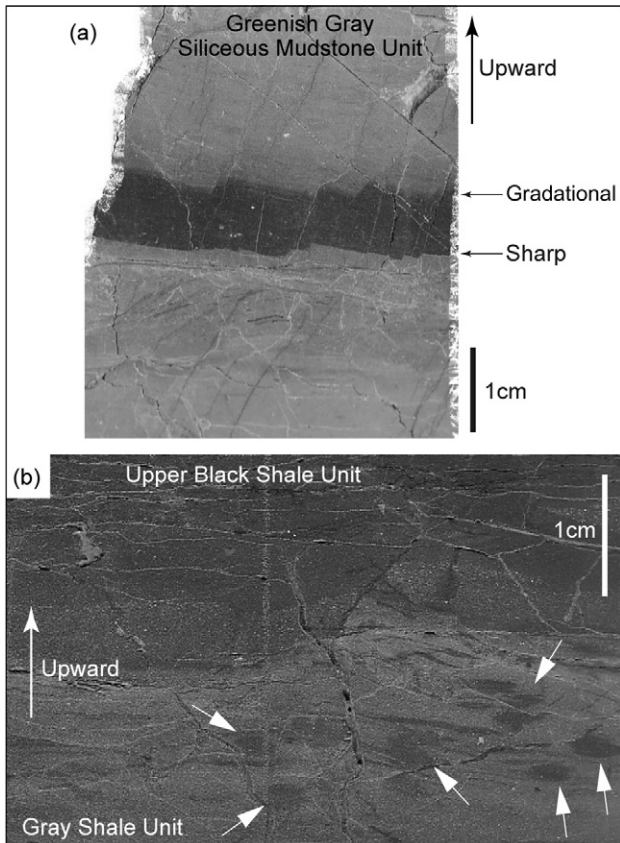


Fig. 7 (a) Stratigraphic direction inferred from the sharp lower and the gradual upper contacts of a thin black shale bed. Color grading around the thin black shale bed is considered to reflect change in concentrations of organic material. Sharp lower contact corresponds to the boundary of depositional environments from oxygen-rich to oxygen-deficient, representing the lack of bioturbation. On the other hand, gradual upper contact corresponds to the boundary of depositional environment from oxygen-deficient to oxygen-rich, representing the influence of bioturbation. Sample was taken from the Greenish Gray Siliceous Mudstone Unit in section MT-3. (b) Stratigraphic direction inferred from black shale filled burrows in gray shale near the boundary between the Gray Shale Unit and the Upper Black Shale Unit in section MT-1. Burrows are indicated by arrows.

Organic carbon isotope stratigraphy for composite pelagic section of the lower Triassic

Measurement of $\delta^{13}\text{C}_{\text{org}}$ was carried out with high temporal resolution for the Lower Triassic continuous pelagic sequence in the Panthalassa (Table 1). Pelagic sedimentary rock samples were obtained from sections MT-1, MT-2, MT-2', MT-3, and MT-4, so as to cover the entire stratigraphic sequence of the lower Triassic. Stratigraphic positions of analyzed samples are shown in Figure 8.

Values of $\delta^{13}\text{C}_{\text{org}}$ range from -34.4 to -21.0‰ with the average of -27.9‰ (Fig. 8). Meter-scale large-amplitude variations are observed throughout the section. In the Lower Black Shale Unit and the lower part of the Gray Shale Unit, the $\delta^{13}\text{C}_{\text{org}}$ values are nearly constant at approximately

-27‰ . The values fluctuate between -30 and -24‰ in the upper part of the Gray Shale Unit and the lower to middle parts of the Upper Black Shale Unit, and gradually decrease to approximately -31‰ toward the upper part of the Upper Black Shale Unit. The $\delta^{13}\text{C}_{\text{org}}$ stays around -30‰ near the base of the Gray Bedded Argillaceous Chert Unit, and gradually increases to approximately -25‰ with relatively large scatter toward the upper part of the Gray Bedded Argillaceous Chert Unit. $\delta^{13}\text{C}_{\text{org}}$ decreases again from -25‰ in the upper part of the Gray Bedded Argillaceous Chert Unit to -30‰ in the upper part of the Greenish Gray Siliceous Mudstone Unit, although it shows a relatively large scatter within the lower part of the Greenish Gray Siliceous Mudstone Unit. The $\delta^{13}\text{C}_{\text{org}}$ abruptly increases to approximately -25‰ in the uppermost part of the Greenish Gray Siliceous Mudstone Unit and stays at around -25‰ in the Red Siliceous Mudstone Unit. From the base of the Gray Bedded Siliceous Mudstone Unit, the $\delta^{13}\text{C}_{\text{org}}$ gradually decreases from -25 to -32‰ toward the black chert bed in the middle part of the Gray Bedded Siliceous Mudstone Unit.

Superimposed on these meter-scale variations in the $\delta^{13}\text{C}_{\text{org}}$ values, tens of centimeter-scale high-amplitude variations, which seem to be related to lithological changes, are also observed. Namely, thin black shale beds tend to decrease ^{13}C as much as 8‰ relative to adjacent gray shale beds in the Gray Shale Unit. A similar relationship is observed between thin black shale intercalations and adjacent argillaceous chert beds in the middle to the upper part of the Gray Bedded Argillaceous Chert Unit, where thin black shale intercalations tend to be depleted in ^{13}C by approximately 3‰ relative to adjacent gray shale beds. On the other hand, thin chert beds in the lower part of the Gray Bedded Argillaceous Chert Unit, the Red Siliceous Mudstone Unit, and the Gray Bedded Siliceous Mudstone Unit tend to be depleted in ^{13}C by approximately 6‰ relative to adjacent argillaceous chert and siliceous mudstone beds. It is possible that samples with higher contents of TOC yielded lower values of $\delta^{13}\text{C}_{\text{org}}$ due to the additional supply of ^{13}C -depleted carbon during early diagenesis created by bacteria in an organic-rich burial environment, contributing to the post-depositional change in the $\delta^{13}\text{C}_{\text{org}}$ values (e.g. Irwin *et al.* 1977). However, it has been well established that the remineralization of organic matter (i.e. respiration of microbes) changes the carbon isotopic composition only slightly (e.g. Lehmann *et al.* 2002). Furthermore, there is no clear relationship between

Table 1 $\delta^{13}\text{C}_{\text{org}}$ and TOC at Inuyama section

| Sample No. | Rock type | Sampling interval [†] (cm) | $\delta^{13}\text{C}_{\text{org}}$ (‰) | TOC (wt%) |
|------------|--------------------|-------------------------------------|--|-----------|
| MT-1 a | Black shale | 5–6 | –26.7 | 0.64 |
| MT-1 b | Black shale | 7–8 | –26.6 | 1.24 |
| MT-1 c | Black shale | 9–10 | –26.7 | 0.37 |
| MT-1 d | Black shale | 11–12 | –26.7 | 0.64 |
| MT-1 e | Gray shale | 12–13 | –27.0 | 0.66 |
| MT-1 f | Gray shale | 14–15 | –26.8 | 0.19 |
| MT-1 g | Gray shale | 15–16 | –27.2 | 0.17 |
| MT-1 h | Gray shale | 18–19 | –27.2 | 0.24 |
| MT-1 3-j | Gray shale | 20–23 | –27.5 | 0.23 |
| MT-1 3-j-k | Gray shale | 24–29 | –23.9 | 0.31 |
| MT-1 3-k | Chert | 28.5–29.5 | –25.5 | 0.24 |
| MT-1 3-l | Chert | 29.5–30.5 | –27.9 | 0.35 |
| MT-1 3-m | Black shale | 37–39 | –30.3 | 6.86 |
| MT-1 3-n | Black shale | 45–47 | –27.5 | 0.35 |
| MT-1 3-n-o | Gray shale | 49–52 | –24.3 | 0.08 |
| MT-1 3-o | Gray shale | 53–56 | –26.3 | 0.65 |
| MT-1 4-a | Black shale | 57–60 | –27.1 | 3.61 |
| MT-1 4-a-b | Black shale | 63–68 | –29.3 | 6.47 |
| MT-1 4-b | Black shale | 72–79 | –25.4 | 3.06 |
| MT-1 4-c | Black shale | 80–85 | –27.3 | 4.54 |
| MT-1 4-d | Black shale | 95–99 | –30.5 | 4.67 |
| MT-1 4-e | Black shale | 108–112 | –30.4 | 4.20 |
| MT-1 4-f | Black shale | 122–126 | –31.7 | 4.73 |
| MT-1 4-g | Black shale | 131–134 | –29.8 | 7.28 |
| MT-1 4-h | Black shale | 139–142 | –30.9 | 2.95 |
| MT-1 4-I | Black shale | 149–153 | –30.7 | 4.67 |
| MT-1 1'-a | Argillaceous chert | 179–181 | –30.9 | 0.05 |
| MT-1 1'-b | Argillaceous chert | 181–182 | –29.4 | 0.05 |
| MT-1 2'-a | Chert | 182–183 | –34.2 | 0.05 |
| MT-1 2'-b | Argillaceous chert | 185–187 | –31.0 | 0.05 |
| MT-1 3' | Argillaceous chert | 187–189 | –30.1 | 0.06 |
| MT-1 4' | Argillaceous chert | 191–192 | –29.1 | 0.03 |
| MT-1 5' | Chert | 194–195 | –34.4 | 0.06 |
| MT-1 6' | Argillaceous chert | 195–196 | –29.8 | 0.04 |
| MT-1 7' | Argillaceous chert | 200–204 | –31.7 | 0.05 |
| MT-1 8' | Argillaceous chert | 207–212 | –29.4 | 0.05 |
| MT-1 9' | Argillaceous chert | 215–219 | –30.0 | 0.07 |
| MT-1 10' | Argillaceous chert | 225–228 | –30.0 | 0.04 |
| MT-1 11' | Argillaceous chert | 232–235 | –30.7 | 0.08 |
| MT-1 12' | Argillaceous chert | 235–238 | –29.5 | 0.04 |
| MT-1 13' | Argillaceous chert | 246–251 | –30.9 | 0.04 |
| MT-2 I-a | Argillaceous chert | 265–268 | –28.8 | 0.04 |
| MT-2 I-b | Black shale | 274–278 | –33.0 | 0.52 |
| MT-2 I-c | Argillaceous chert | 281–285 | –28.6 | 0.05 |
| MT-2 I-d | Black shale | 299–300 | –32.0 | 1.29 |
| MT-2 II | Argillaceous chert | 302–304 | –30.5 | 0.10 |
| MT-2 III | Argillaceous chert | 304–306 | –28.2 | 0.04 |
| MT-2 IV | Argillaceous chert | 319–312 | –29.4 | 0.03 |
| MT-2 14 | Argillaceous chert | 316–319 | –28.8 | 0.06 |
| MT-2 15-a | Argillaceous chert | 323–327 | –28.0 | 0.05 |
| MT-2 15-b | Argillaceous chert | 332–335 | –30.0 | 0.04 |
| MT-2 16-a | Argillaceous chert | 340–344 | –28.8 | 0.03 |
| MT-2 16-b | Black shale | 348–352 | –32.2 | 1.00 |
| MT-2 17 | Argillaceous chert | 359–364 | –31.9 | 0.05 |
| MT-2 18-a | Argillaceous chert | 376–380 | –29.8 | 0.02 |
| MT-2 18-b | Chert | 383–387 | –28.7 | 0.04 |
| MT-2 19 | Argillaceous chert | 389–395 | –26.1 | 0.10 |
| MT-2 20 | Argillaceous chert | 403–407 | –28.7 | 0.04 |
| MT-2' 24 | Argillaceous chert | 423–426 | –25.8 | 0.18 |
| MT-2' 25 | Argillaceous chert | 434–438 | –24.9 | 0.18 |
| MT-2' 26 | Argillaceous chert | 443–446 | –25.0 | 0.16 |
| MT-2' 27-a | Black shale | 455–457 | –31.2 | 1.51 |
| MT-3 a | Argillaceous chert | 485–487 | –28.2 | 0.06 |

Table 1 *Continued*

| Sample No. | Rock type | Sampling interval [†] (cm) | $\delta^{13}\text{C}_{\text{org}}$ (‰) | TOC (wt%) |
|------------|--------------------|-------------------------------------|--|-----------|
| MT-3 b | Argillaceous chert | 488–490 | –29.1 | 0.08 |
| MT-3 c | Black shale | 494–496 | –30.8 | 1.58 |
| MT-3 d | Siliceous mudstone | 499–505 | –25.7 | 0.03 |
| MT-3 e | Siliceous mudstone | 506–512 | –28.4 | 0.09 |
| MT-3 f | Siliceous mudstone | 512–517 | –29.5 | 0.08 |
| MT-3 5U | Siliceous mudstone | 521–525 | –29.0 | 0.07 |
| MT-3 5 L | Siliceous mudstone | 529–530 | –25.4 | 0.03 |
| MT-3 4U | Siliceous mudstone | 531–534 | –27.9 | 0.14 |
| MT-3 4 L | Siliceous mudstone | 535–538 | –28.0 | 0.17 |
| MT-3 2 | Argillaceous chert | 538–539 | –29.2 | 0.16 |
| MT-3 3U | Siliceous mudstone | 541–546 | –27.3 | 0.07 |
| MT-3 12 | Siliceous mudstone | 548–551 | –21.0 | 0.19 |
| MT-3 13 | Siliceous mudstone | 553–555 | –26.1 | 0.18 |
| MT-3 14 | Siliceous mudstone | 555–559 | –28.2 | 0.42 |
| MT-3 15 | Siliceous mudstone | 560–564 | –26.0 | 0.13 |
| MT-3 16 | Black shale | 564–565 | –29.1 | 1.01 |
| MT-3 17 | Siliceous mudstone | 573–578 | –27.5 | 0.19 |
| MT-4 1 | Siliceous mudstone | 582–586 | –28.4 | 0.05 |
| MT-4 3 | Siliceous mudstone | 587–590 | –28.5 | 0.05 |
| MT-4 5 | Siliceous mudstone | 601–604 | –29.8 | 0.08 |
| MT-4 6 | Siliceous mudstone | 607–610 | –28.7 | 0.09 |
| MT-4 7 | Siliceous mudstone | 617–619 | –29.7 | 0.05 |
| MT-4 8 | Siliceous mudstone | 620–623 | –25.0 | 0.03 |
| MT-4 9 | Siliceous mudstone | 624–627 | –26.4 | 0.04 |
| MT-4 10 | Chert | 628–629 | –32.6 | 0.03 |
| MT-4 11 | Siliceous mudstone | 634–638 | –29.7 | 0.14 |
| MT-4 c | Siliceous mudstone | 651–655 | –26.7 | 0.03 |
| MT-4 d | Chert | 657–658 | –32.5 | 0.02 |
| MT-4 e | Siliceous mudstone | 661–666 | –25.3 | 0.03 |
| MT-4 79 | Siliceous mudstone | 694–696 | –24.9 | 0.03 |
| MT-4 80 | Siliceous mudstone | 699–701 | –24.5 | 0.04 |
| MT-4 81 | Siliceous mudstone | 704–709 | –25.1 | 0.04 |
| MT-4 82 | Chert | 710–712 | –29.7 | 0.11 |
| MT-4 83 | Siliceous mudstone | 719–724 | –25.7 | 0.03 |
| MT-4 84 | Siliceous mudstone | 727–731 | –25.5 | 0.04 |
| MT-4 85 | Siliceous mudstone | 736–739 | –27.8 | 0.13 |
| MT-4 86 | Siliceous mudstone | 743–748 | –28.1 | 0.15 |
| MT-4 87 | Siliceous mudstone | 754–758 | –27.9 | 0.11 |
| MT-4 88 | Chert | 762–764 | –30.7 | 0.02 |
| MT-4 90 | Siliceous mudstone | 767–770 | –29.5 | 0.04 |
| MT-4 92 | Siliceous mudstone | 775–779 | –28.6 | 0.02 |
| MT-4 94 | Siliceous mudstone | 798–801 | –31.3 | 0.27 |
| MT-4 96 | Chert | 807–808 | –31.3 | 0.07 |
| MT-4 98 | Chert | 814–815 | –31.8 | 0.21 |
| MT-4 100 | Chert | 828–830 | –27.4 | 0.39 |

[†] Stratigraphic interval corresponding to the composite columnar section shown in Figure 8.
TOC, total organic carbon.

TOC and the $\delta^{13}\text{C}_{\text{org}}$ values among all samples, suggesting that $\delta^{13}\text{C}_{\text{org}}$ values did not depend on the post-depositional environment. Therefore, these might represent short-term changes in dominant species of primary producers in the surface-water on the scale of 10^4 years.

TOC contents are generally high with an average value of 3.5wt% in the Lower and the Upper Black Shale Units, whereas those of intercalated thin black shale beds in the Gray Shale Unit, the Gray Bedded Argillaceous Chert Unit,

and the Greenish Gray Siliceous Mudstone Unit, are generally between 1.0 and 1.5wt%. TOC contents in other lithologies are generally less than 0.5wt%.

DISCUSSION

In order to establish the age model for the Lower Triassic pelagic sequence in the Inuyama area, we correlated the stratigraphic variation pattern

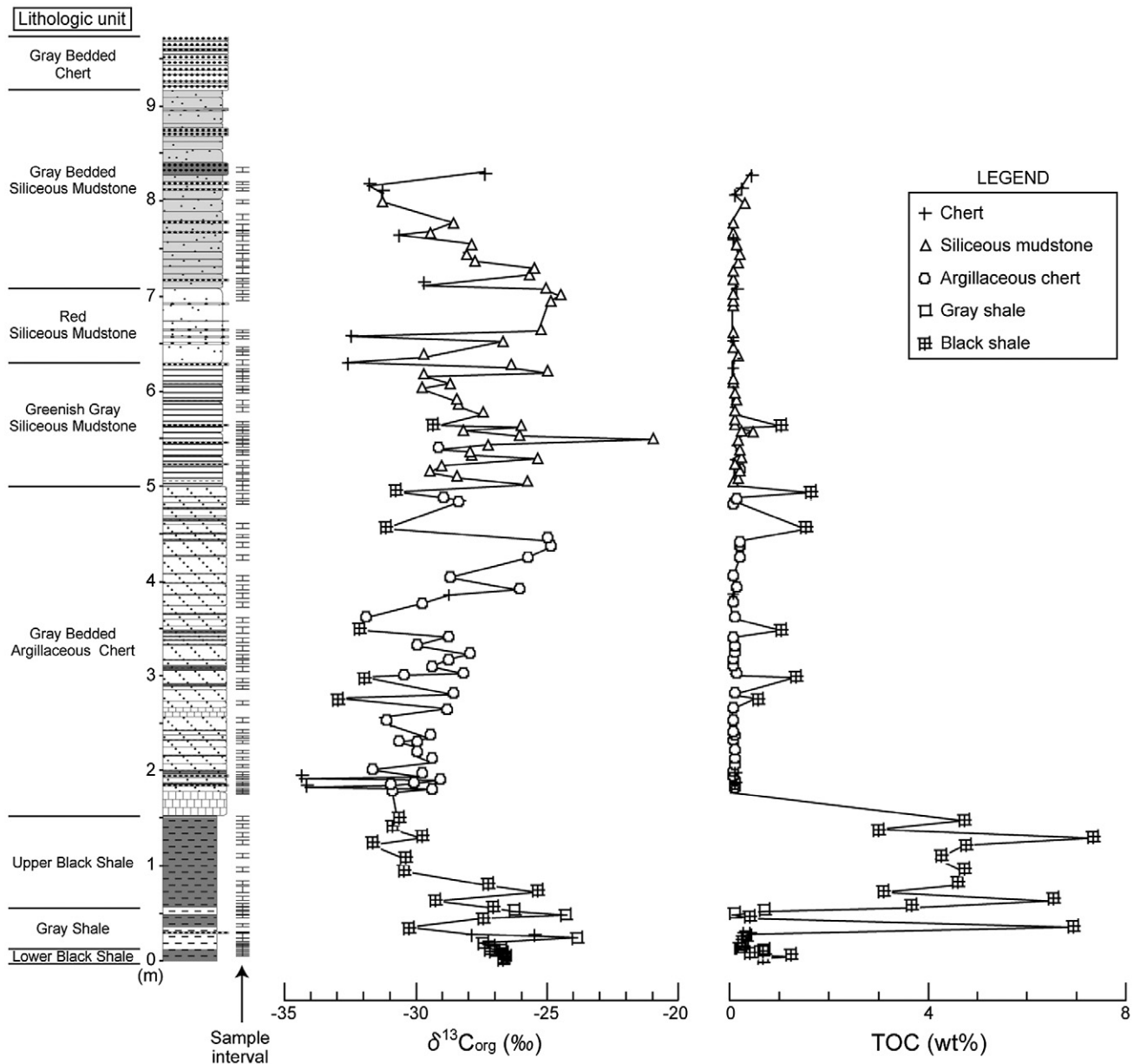


Fig. 8 Stratigraphic variations of $\delta^{13}\text{C}_{\text{org}}$ and total organic carbon for the reconstructed sequence at Inuyama section. Sampling intervals are indicated to the right of the composite column.

of $\delta^{13}\text{C}_{\text{org}}$ obtained in this study with 'standard' carbonate carbon isotope records of Lower Triassic (Fig. 9). We used carbonate carbon isotopic ($\delta^{13}\text{C}_{\text{carb}}$) records of Payne *et al.* (2004) and Galfetti *et al.* (2007a) as target records, because these records have high resolution and cover the Early Triassic period with a detailed well-constrained time framework based on conodont (Payne *et al.* 2004) and ammonoid (Galfetti *et al.* 2007a) biostratigraphy, and U–Pb ages (Mundil *et al.* 2004; Ovtcharova *et al.* 2006; Galfetti *et al.* 2007a). Materials for measurements are mainly from

shallow-marine limestone deposited in the tropical Tethys, obtained from the Guizhou (Payne *et al.* 2004) and Guangxi (Galfetti *et al.* 2007a) areas in southern China.

Although some differences in amplitude of $\delta^{13}\text{C}_{\text{carb}}$ variations in the two sections could have resulted from calcification of the depth-dependent ^{13}C -depleted dissolved inorganic carbon formed by respiration of organic matter (Cao *et al.* 2010), million-year-scale large-amplitude oscillations of $\delta^{13}\text{C}_{\text{carb}}$ are still observable during the Lower Triassic, as follows.

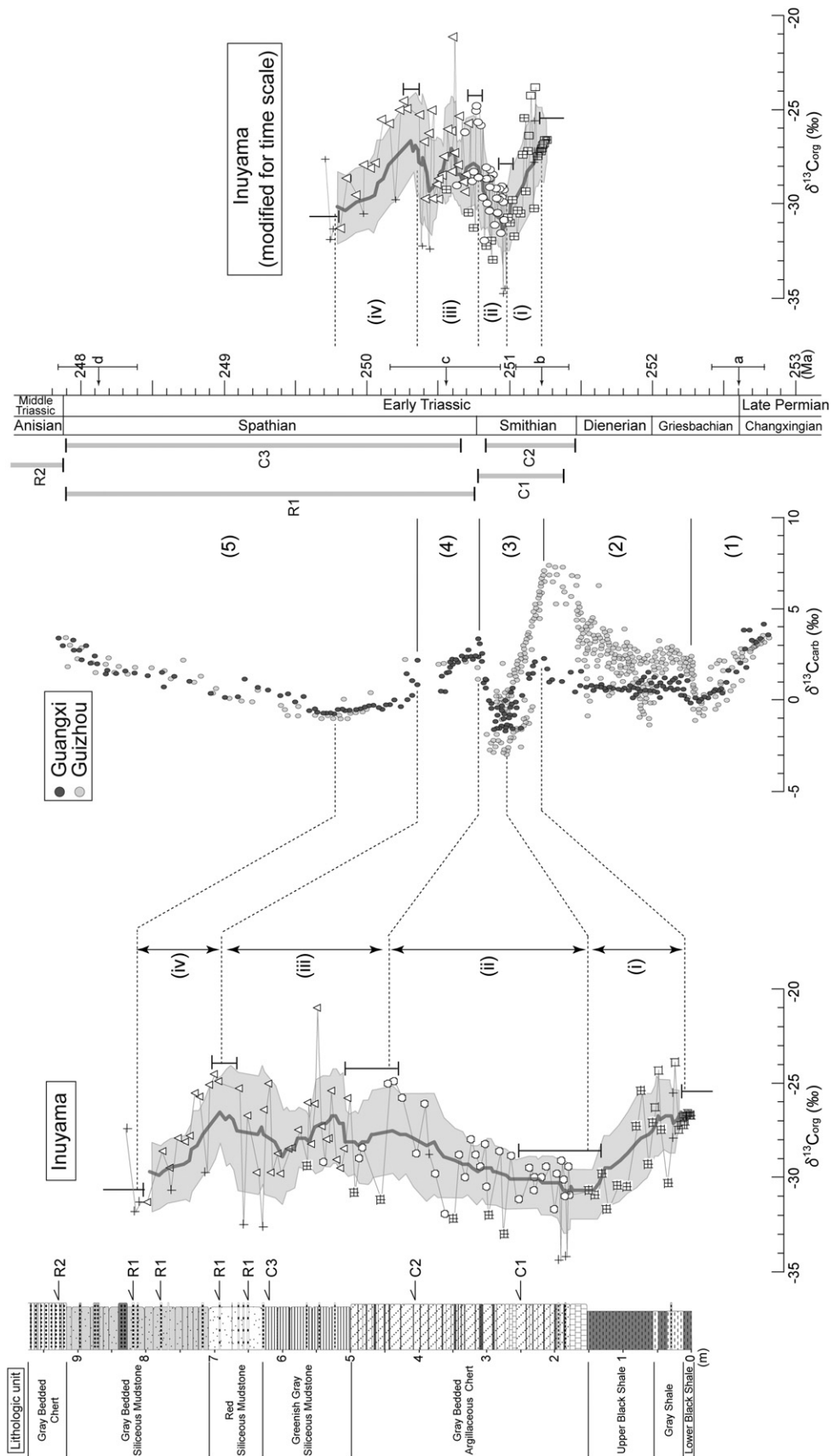


Fig. 9 Correlation of carbon isotopic curve for Inuyama section with those for southern China (Guizhou, Payne *et al.* 2004; and Guanzhou, Galfetti *et al.* 2007a). Symbols are the same as in Fig. 8. Dark gray bold line and light gray shade in $\delta^{13}\text{C}_{\text{org}}$ data of Inuyama section represent a 10-point moving average and a standard deviation ($\pm \sigma$) of those 10-points that are used to calculate the average value, respectively. Time scale for the Early Triassic is after Galfetti *et al.* (2007a) with U–Pb ages of 252.6 ± 0.2 Ma (Mundil *et al.* 2004) for a, 251.22 ± 0.20 Ma (Galfetti *et al.* 2007a) for b, 250.55 ± 0.40 Ma (Ovcharova *et al.* 2006) for c, and 248.12 ± 0.28 Ma (Ovcharova *et al.* 2006) for d. Occurrence horizons of age diagnostic radiolarian (R1, R2) and conodont (C1, C2, C3) fossils are indicated by arrows on the right side of the composite column (Yao & Kuwahara 1997; Takahashi *et al.* 2009b; Yamakita *et al.* 2010), and their occurrence ranges are indicated by vertical bars on the left side of the time scale (Sugiyama 1992; Orchard 1995, 2007; Yao & Kuwahara 1997). Dotted lines represent correlation of carbon isotopic records based on the similarity in general variation trends of carbon isotopic curves. The general variation pattern in $\delta^{13}\text{C}_{\text{carb}}$ in stratigraphic intervals of (1), (2), (3), (4), and (5), and the basis of $\delta^{13}\text{C}$ correlation in the intervals of (i), (ii), (iii), and (iv) are described in the text. The diagram of $\delta^{13}\text{C}_{\text{org}}$ variation vs geological age in the center is based on the results of the correlation on the right side. See text for further explanation.

- 1 An abrupt decrease in $\delta^{13}\text{C}_{\text{carb}}$ from approximately +4 to -1‰ across the P–T boundary, which is followed by an abrupt increase to +1 to $+2\text{‰}$ during the lower Griesbachian.
- 2 A positive shift by 2 to 8‰ toward the lowermost Smithian. It is worth noting that the amplitude is different between sections.
- 3 A decrease to approximately -2‰ from the lowermost Smithian to the upper Smithian and then an increase to $+2\text{‰}$ toward the uppermost Smithian.
- 4 A decrease to approximately -1‰ from the lowermost Spathian to the lower Spathian, which is followed by an increase to $+2\text{‰}$ during the lower Spathian.
- 5 Negative and then positive shifts with an amplitude of approximately 4‰ from the lower Spathian to the uppermost Spathian.

Thus, million-year-scale large-amplitude oscillations characterize the $\delta^{13}\text{C}_{\text{carb}}$ variation pattern in the Lower Triassic.

In addition to these two sections in south China, $\delta^{13}\text{C}_{\text{carb}}$ records showing similar variation patterns have been obtained from other P–T boundary to the Lower Triassic sections in the Tethys such as Salt Range (Baud *et al.* 1996), Carnic Alps (Holser *et al.* 1989), and Iran (Horacek *et al.* 2007). These results strongly suggest that the $\delta^{13}\text{C}_{\text{carb}}$ variation pattern compiled above represents geochemical signals at least on the Tethyan-wide scale, which should reflect changes in the atmospheric and surface ocean $\delta^{13}\text{C}$ during the Early Triassic on the global scale (e.g. Horacek *et al.* 2007; Yin *et al.* 2007). Furthermore, $\delta^{13}\text{C}_{\text{org}}$ data show variation patterns similar to those during the end-Permian to Griesbachian at Carnic Alps (Magaritz *et al.* 1992) and Southwest Japan (Musashi *et al.* 2001) and from the Smithian to Spathian at Barents Sea (Galfetti *et al.* 2007b). Therefore, it is reasonable to correlate $\delta^{13}\text{C}_{\text{org}}$ profiles of Panthalassa with $\delta^{13}\text{C}_{\text{carb}}$ profiles of Tethys.

Correlation of carbon isotope profiles between the Inuyama section and south China was conducted by the following procedure. First, we applied biostratigraphic constraints based on occurrences of three conodont fossils and two radiolarian zones to construct an age model of the Inuyama section. The range of *Neospathodus bransoni* is considered as middle to late Smithian (Orchard 2007) that occurs in the lower part of the Gray Bedded Argillaceous Chert Unit (C1 in Fig. 9; Yamakita *et al.* 2010). The range of *Neogondolella milleri* is considered as early to middle Smithian (Orchard 2007) which occurs in the

upper part of the Gray Bedded Argillaceous Chert Unit (C2 in Fig. 9; Yamakita *et al.* 2010). The range of *Neospathodus symmetricus* is considered as almost entire Spathian (Orchard 1995) which occurs in the upper part of the Greenish Gray Siliceous Mudstone Unit (C3 in Fig. 9; Takahashi *et al.* 2009b). The range of *Parentactinia nakatsugawaensis* zone is considered as almost entirely Spathian (Yao & Kuwahara 1997) which occurs in the Red Siliceous Mudstone Unit and Gray Bedded Siliceous Mudstone Unit (R1 in Fig. 9; Yao & Kuwahara 1997). The range of *Hozmadia gifuensis* zone is considered as early Anisian (Sugiyama 1992) which occurs in the Gray Bedded Chert Unit (R2 in Fig. 9; Yao & Kuwahara 1997). Based on these age constraints, the lithological interval from the Red Siliceous Mudstone Unit to the Gray Bedded Siliceous Mudstone Unit is correlated to the Spathian, and the Gray Bedded Chert Unit is correlated to the Anisian, respectively.

A ten-point moving average of $\delta^{13}\text{C}_{\text{org}}$ was taken to demonstrate the general variation pattern of $\delta^{13}\text{C}_{\text{org}}$ (Fig. 9). Within the Smithian and the Spathian, the $\delta^{13}\text{C}_{\text{org}}$ profile for the Inuyama section can be correlated with the $\delta^{13}\text{C}_{\text{carb}}$ profile for shallow-marine sequences in south China based on the similarity in variation patterns (stratigraphic intervals (i–iv) in Fig. 9) as follows.

- 1 The decrease in $\delta^{13}\text{C}_{\text{org}}$ from approximately -27‰ in the lowermost part of the Gray Shale Unit to approximately -31‰ in the uppermost part of the Upper Black Shale Unit is correlated with the decrease in $\delta^{13}\text{C}_{\text{carb}}$ in the lower to middle Smithian interval ((i) in Fig. 9).
- 2 More or less constant $\delta^{13}\text{C}_{\text{org}}$ values of approximately -30‰ and the following increase to approximately -25‰ from the base of the Gray Bedded Argillaceous Chert Unit to the upper part of the Gray Bedded Argillaceous Chert Unit is correlated with the increase in $\delta^{13}\text{C}_{\text{carb}}$ from the middle Smithian toward the uppermost Smithian interval ((ii) in Fig. 9).
- 3 The decrease in $\delta^{13}\text{C}_{\text{org}}$ to approximately -30‰ in the upper part of the Greenish Gray Siliceous Mudstone Unit and the following increase to approximately -25‰ in the upper part of the Red Siliceous Mudstone Unit is correlated with the decrease and the following increase in $\delta^{13}\text{C}_{\text{carb}}$ in the lowermost Spathian interval ((iii) in Fig. 9).
- 4 The decrease in $\delta^{13}\text{C}_{\text{org}}$ to approximately -31‰ in the middle part of the Gray Bedded Siliceous Mudstone Unit is correlated with the gradual

decrease in $\delta^{13}\text{C}_{\text{carb}}$ in the lower Spathian interval (iv) in Fig. 9).

The duration of the $\delta^{13}\text{C}_{\text{org}}$ profile is linearly interpolated for each stratigraphic interval of (i), (ii), (iii), and (iv). However, stratigraphic positions of age-control points described in Figure 9 have uncertainties in correlation with the $\delta^{13}\text{C}_{\text{carb}}$ curves because of the relatively large scatter and rather gradual shifts in the $\delta^{13}\text{C}_{\text{org}}$ values at Inuyama section. The uncertainties in correlation are given as bars in Figure 9.

Average sedimentation rates for the stratigraphic intervals (i), (ii), (iii), and (iv) were calculated based on their thickness and corresponding time duration, which can be estimated from U–Pb ages on the carbonate sequence at Guangxi, southern China (Galfetti *et al.* 2007a). Galfetti *et al.* (2007a) identified four stages, Griesbachian, Dinerian, Smithian, and Spathian, during the Early Triassic based on detailed ammonoid biostratigraphy. They also determined three numerical ages 251.22 ± 0.20 , 250.55 ± 0.40 , and 248.12 ± 0.28 Ma during the Early Triassic on volcanic ash layers in the carbonate sequence at Guangxi based on U–Pb geochronology (Ovtcharova *et al.* 2006; Galfetti *et al.* 2007a). In addition, the U–Pb age of the P–T boundary was estimated to be 252.6 ± 0.20 Ma on volcanic ash layers at Shangsi and Meishan, southern China (Mundil *et al.* 2004).

The average sedimentation rate for interval (i), from the Gray Shale Unit to the Upper Black Shale Unit in the middle Smithian, is estimated to be approximately 5.6 m/my (1.6–14 m/my) (Fig. 10) based on the thickness of approximately 1.4 m and its corresponding time duration of 0.25 ± 0.60 my (Galfetti *et al.* 2007a). The average sedimentation rate for the interval (ii), from the base of the Gray Bedded Argillaceous Chert Unit to the upper part of the Gray Bedded Argillaceous Chert Unit, in the upper Smithian is estimated to be approximately 15.0 m/my (3.8–30 m/my) (Fig. 10) based on the thickness of approximately 3.0 m and its corresponding time duration of 0.20 ± 0.60 my (Galfetti *et al.* 2007a). The average sedimentation rate for interval (iii), from the upper part of the Gray Bedded Argillaceous Chert Unit to the upper part of the Red Siliceous Mudstone Unit, in the lowermost Spathian is estimated to be approximately 5.1 m/my (1.8–23 m/my) (Fig. 10) based on the thickness of approximately 2.3 m and its corresponding time duration of 0.45 ± 0.80 my (Galfetti *et al.* 2007a). The average sedimentation rate for interval (iv), from the upper part of the Red Siliceous Mudstone Unit to the middle part of the Gray

Siliceous Mudstone Unit, in the lower Spathian is estimated to be approximately 2.5 m/my (1.1–14 m/my) (Fig. 10) based on the thickness of approximately 1.4 m and its corresponding time duration of 0.55 ± 0.68 my (Galfetti *et al.* 2007a).

The study on the Middle and Upper Triassic and Lower Jurassic radiolarian bedded chert in the Inuyama area revealed that a chert–shale couplet is representing the average duration of 20 ky, suggesting the possibility of its precession origin (Hori *et al.* 1993; Ikeda *et al.* 2010a, b). Ikeda *et al.* (2010a, b) further demonstrated that the sedimentary rhythms of the bedded chert are of astronomical cycle origin based on their hierarchical cyclicity of chert bed thickness variation. Although it is not yet demonstrated that the sedimentary rhythms of the lower Triassic sequence is also of astronomical cycle origin, such an origin is highly likely considering their downward continuity from the Middle Triassic sequence studied by Ikeda *et al.* (2010a). So, we assume that a couplet of either chert–shale or siliceous shale–shale couplet in the lower Triassic sequence also represents a precession cycle, and test whether this assumption is consistent with the age model described above.

The Gray Bedded Argillaceous Chert Unit and the Greenish Gray Siliceous Mudstone Unit from the upper Smithian to the lowermost Spathian are characterized by periodic intercalations of thin black shale beds. Assuming that thin bed couplets of siliceous mudstone–black shale, or argillaceous chert–black shale reflect approximately 20 ky precession cyclicity, sedimentation rates for the Gray Bedded Argillaceous Chert Unit and the Greenish Gray Siliceous Mudstone Unit are estimated to be 7.1 and 11.3 m/my, respectively (Fig. 10), because average thicknesses of one couplet are 14.2 cm for the Gray Bedded Argillaceous Chert Unit and 22.5 cm for the Greenish Gray Siliceous Mudstone Unit, respectively. Although the estimated sedimentation rate of 11.3 m/my for the Greenish Gray Siliceous Mudstone Unit is somewhat higher than the rate estimated for interval (iii) including the Greenish Gray Siliceous Mudstone Unit by using the carbon isotope stratigraphy, these estimated sedimentation rates are consistent with the latter estimates, considering the errors based on the carbon isotope stratigraphy (Fig. 10).

The stratigraphic interval from the Red Siliceous Mudstone Unit to the Gray Bedded Siliceous Mudstone Unit of the lower Spathian is characterized by alternations of siliceous mudstone or chert and shale beds. Assuming that a siliceous mudstone–shale or chert–shale couplet reflects an

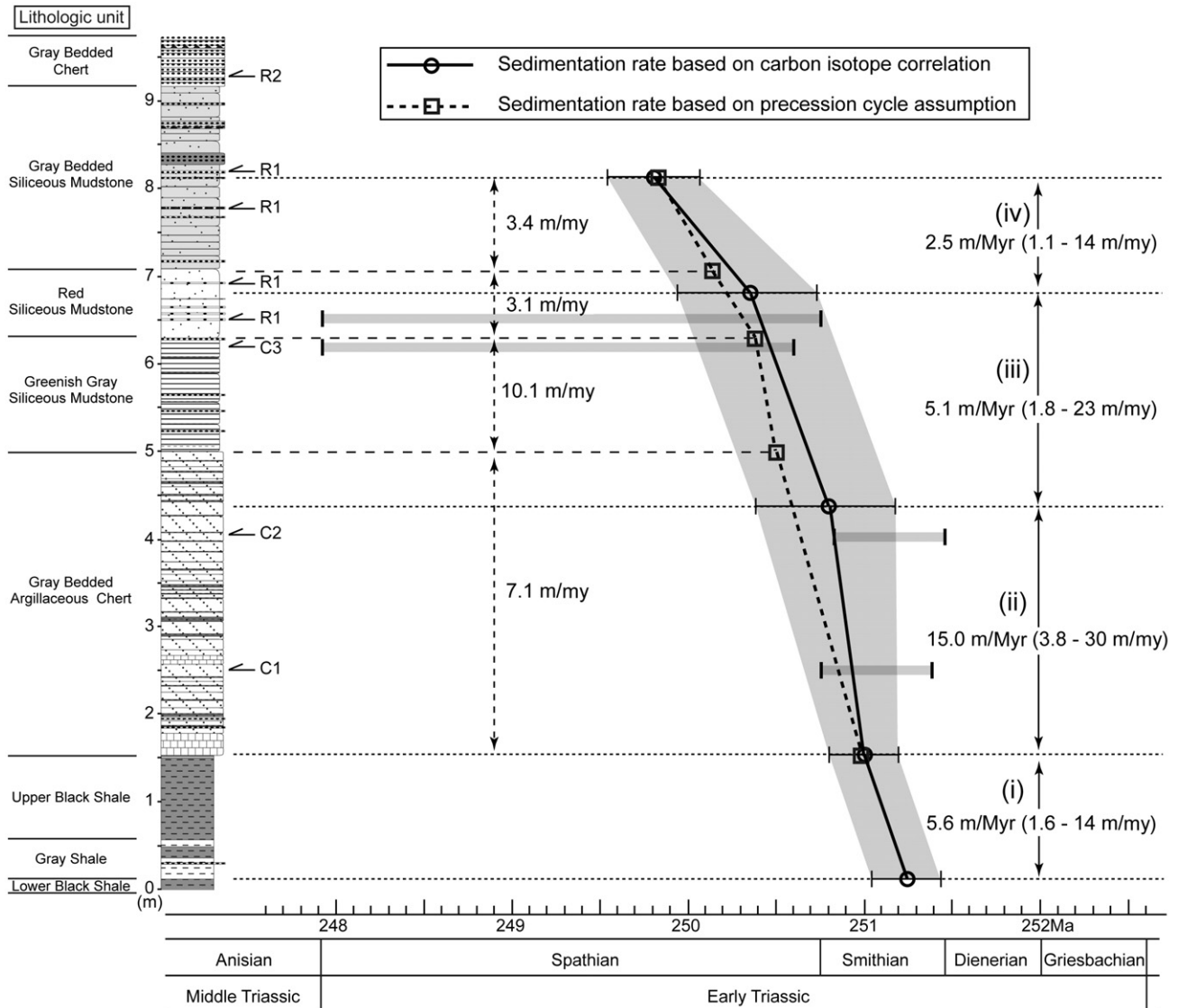


Fig. 10 Sedimentation diagram of the reconstructed sequence at Inuyama section based on the correlation of carbon isotope stratigraphy (○) and on the assumptions that an approximately 20 ky precession cycle (□) is represented by the time duration for a couplet of thin black shale bed-siliceous part in the Gray Bedded Argillaceous Chert Unit and the Greenish Gray Siliceous Mudstone Unit, and for a couplet of siliceous mudstone-shale or chert-shale in the Red Siliceous Mudstone Unit and the Gray Bedded Siliceous Mudstone Unit. Arrows indicate the horizons of age-diagnostic radiolarian (R1, R2) and conodont (C1, C2, C3) fossils and the thick gray horizontal bars represent their ranges.

approximately 20-ky precession cyclicity, sedimentation rates for the Red Siliceous Mudstone Unit and the lower part of the Gray Siliceous Mudstone Unit are estimated to be 3.1 and 3.4 m/my, respectively (Fig. 10), based on average thicknesses of one couplet of 6.2 and 6.8 cm, respectively, for each stratigraphic interval. These estimated sedimentation rates are consistent within errors with the age constraints based on the correlation using carbon isotope stratigraphy (Fig. 10).

It is evident from the above estimates that the sedimentation rate for the upper Smithian (approximately 15 m/my) is much higher than

those for the lower Smithian (approximately 5.6 m/my), the lowermost to lower Spathian (approximately 5.1 to 2.5 m/my), and the Middle Triassic – Lower Jurassic bedded chert (1 to 4 m/my; e.g. Matsuda & Isozaki 1991; Ikeda *et al.* 2010a). The sedimentary sequence exposed at Inuyama section is characterized by pelagic siliceous sedimentary rocks deposited on the oceanic crust of the low latitude Panthalassa (e.g. Matsuda & Isozaki 1991). Therefore, up to a 10-fold increase in sedimentation rate during the late Smithian would have been caused either by the drastic increase in biogenic silica accumulation rate or the eolian dust

accumulation rate. Because the upper Smithian sequence is characterized by more argillaceous lithologies, the observed higher sedimentation rates during the late Smithian should imply more than a ten-fold increase in terrigenous input to the pelagic ocean during this period based on the comparison of sedimentation rate of the upper Smithian (approximately 16 m/my) with the Middle Triassic (approximately 2.0 m/my; Ikeda *et al.* 2010a) at the Inuyama section.

Although palynological and paleobotanical records of the Early Triassic are fragmental, especially in low latitudes, they tend to suggest that extremely devastating terrestrial ecosystems continued after the P–T boundary (e.g. Looy *et al.* 1999). According to palynological studies from European continent in low- to mid-latitude northern hemisphere (Looy *et al.* 1999) and the Boreal realm, which was located around 50°N (Galfetti *et al.* 2007b) during the Early Triassic, gymnosperm diversity seems to have recovered since the Spathian. In addition, palynological data about the xerophyte–hygrophyte element ratio from the Boreal realm indicate that highly dry climatic conditions were dominant during the late Smithian, with shifts to a more humid climate in the Spathian (Galfetti *et al.* 2007b). Recently, it is demonstrated that the higher bulk accumulation rate during the Griesbachian to Dienerian relative to the Changxingian (latest Permian) is observed from various sections in continent-margin and platform sediments, and the sedimentation rate continued to be high up to the Smithian in Meishan and Chaohu, shallow-water Tethys (Algeo & Twitchett 2010). These changes in sediment fluxes suggest a large increase in the eroded materials from adjacent land areas due to accelerated rates of chemical and physical weathering as a function of higher surface temperatures, increased acidity of precipitation, and changes in landscape stability tied to destruction of terrestrial ecosystems during the Early Triassic (Algeo & Twitchett 2010). Our data imply increased physical weathering and dust emission rates from the continent in the northern hemisphere during the late Smithian, which might have resulted in the drastic increase in eolian dust accumulation in the pelagic realm during the Smithian more than the Griesbachian to Dienerian.

CONCLUSIONS

1 High-resolution continuous reconstruction of the Lower Triassic pelagic sequence was con-

ducted at the Inuyama section, central Japan, based on detailed field mapping, construction of columnar sections for each fault-bounded block, and lithostratigraphic correlations of the columnar sections. The reconstructed sequence is approximately 9.5 m thick, and is composed of eight lithological units: Lower Black Shale Unit, Gray Shale Unit, Upper Black Shale Unit, Gray Bedded Argillaceous Chert Unit, Greenish Gray Siliceous Mudstone Unit, Red Siliceous Mudstone Unit, Gray Siliceous Mudstone Unit, and Gray Bedded Chert Unit, in ascending order.

- 2 Measurement of $\delta^{13}\text{C}_{\text{org}}$ was conducted for the reconstructed pelagic sequence with high temporal resolution. Stratigraphic variations in $\delta^{13}\text{C}_{\text{org}}$ generally show large-amplitude fluctuations between -34.4 and -21.0‰ throughout the sequence.
- 3 In order to construct the age model for the Lower Triassic pelagic sequence, a correlation was conducted between the $\delta^{13}\text{C}_{\text{org}}$ profile at Inuyama section and the high-resolution $\delta^{13}\text{C}_{\text{carb}}$ profile from southern China using conodont and radiolarian biostratigraphy as age constraints.
- 4 The correlation provides a well-controlled age framework for the pelagic sequence of Panthalassa from the Smithian to the Spathian. The result reveals the extremely high terrigenous sedimentation rate during the upper Smithian, which likely resulted from the increased eolian dust input from Pangea.

ACKNOWLEDGEMENTS

We thank Dr Y. Isozaki and Dr S. Yamakita for their advice on field research, reconstruction of lithostratigraphy, and the age model for this study. This research is a part of the doctoral thesis of HS under the guidance of RT, and was financially supported by Grant-in-Aid of the Fukada Geological Institute and Fujiwara Natural History Foundation awarded to HS.

REFERENCES

- ALGEO T. J. & TWITCHETT R. J. 2010. Anomalous Early Triassic sediment fluxes due to elevated weathering rates and their biological consequences. *Geology* **38**, 1023–6.
- ALGEO T. J., HINNOV L., MOSER J. *et al.* 2010. Changes in productivity and redox conditions in the Panthalassic Ocean during the latest Permian. *Geology* **38**, 187–90.

- ANDO A., KODAMA K. & KOJIMA S. 2001. Low-latitude and Southern Hemisphere origin of Anisian (Triassic) bedded chert in the Inuyama area, Mino terrane, central Japan. *Journal of Geophysical Research* **106**, 1973–86.
- BAUD A., ATUDOREI V. & SHARP Z. 1996. Late Permian and Early Triassic evolution of the northern Indian margin. *Geodinamica Acta* **9**, 57–77.
- CAO C. Q., YANG Y. C., SHEN S. Z., WANG W., ZHENG Q. F. & SUMMONS R. E. 2010. Pattern of $\delta^{13}\text{C}_{\text{carb}}$ and implications for geological events during the Permian-Triassic transition in South China. *Geological Journal* **45**, 186–94.
- ERWIN D. H. 1994. The Permo-Triassic extinction. *Nature* **367**, 231–6.
- FLÜGEL E. 2002. Triassic reef patterns. In Kiessling W., Flügel E. and Golonka J. (eds.) *Phanerozoic Reef Patterns*, pp. 391–463, Society for Sedimentary Geology (SEPM) Special Publication **72**, SEPM, Tulsa, OK.
- GALFETTI T., BUCHER H., OVTCHAROVA M. *et al.* 2007a. Timing of the Early Triassic carbon cycle perturbations inferred from new U-Pb ages and ammonoid biochronozones. *Earth and Planetary Science Letters* **258**, 593–604.
- GALFETTI T., HOCHULI P. A., BRAYARD A., BUCHER H., WEISSERT H. & VIGRAN J. O. 2007b. Smithian-Spathian boundary event: Evidence for global climatic change in the wake of the end-Permian biotic crisis. *Geology* **35**, 291–4.
- HOLSER W. T., SCHÖNLAUB H. P., ATTREP M. *et al.* 1989. A unique geochemical record at the Permian/Triassic boundary. *Nature* **337**, 39–44.
- HORACEK M., RICHOSZ S., BRANDNER R., KRISTYN L. & SPOTL C. 2007. Evidence for recurrent changes in Lower Triassic oceanic circulation of the Tethys: The $\delta^{13}\text{C}$ record from marine sections in Iran. *Palaeogeography, Palaeoclimatology, Palaeoecology* **252**, 355–69.
- HORI R. S., CHO C. F. & UMEDA H. 1993. Origin of cyclicity in Triassic-Jurassic radiolarian bedded cherts of the Mino accretionary complex from Japan. *Island Arc* **3**, 170–80.
- IKEDA M., TADA R. & SAKUMA H. 2010a. Astronomical cycle origin of bedded chert: A middle Triassic bedded chert sequence, Inuyama, Japan. *Earth and Planetary Science Letters* **297**, 369–78.
- IKEDA M., TADA R., KARASUDA A. & SAKUMA H. 2010b. Long-period astronomical cycles from the Upper Triassic to Lower Jurassic Bedded Chert sequence: Implications for Jurassic cyclostratigraphy. *Earth Science Frontiers* **17**, 112–3.
- IRWIN H., CURTIS C. D. & COLEMAN M. 1977. Isotopic evidence for source of diagenetic carbonates formed during burial of organic-rich sediments. *Nature* **269**, 209–13.
- ISOZAKI Y. 1997. Permo-Triassic boundary superanoxia and stratified superocean: Records from lost deep sea. *Science* **276**, 235–8.
- KAJIWARA Y., YAMAKITA S., ISHIDA K., ISHIGA H. & IMAI A. 1994. Development of a largely anoxic stratified ocean and its temporary massive mixing at the Permian/Triassic boundary supported by the sulfur isotopic record. *Palaeogeography, Palaeoclimatology, Palaeoecology* **111**, 367–79.
- KAKUWA Y. 2008. Evaluation of palaeo-oxygenation of the ocean bottom across the Permian-Triassic boundary. *Global and Planetary Change* **63**, 40–56.
- KATO Y., NAKAO K. & ISOZAKI Y. 2002. Geochemistry of Late Permian to Early Triassic pelagic cherts from southwest Japan: Implications for an oceanic redox change. *Chemical Geology* **182**, 15–34.
- KIMURA K. & HORI R. 1993. Offscraping accretion of Jurassic chert-clastic complex in the Mino-Tamba Belt, central Japan. *Journal of Structural Geology* **15**, 145–61.
- KUWAHARA K. & YAMAKITA S. 2001. Microbiostratigraphy on chert faces of Upper Permian in the Northern Chichibu Belt, Shikoku, Southwest Japan. *News of Osaka Micropaleontology, Special Volume* **12**, 51–69 (in Japanese with English abstract).
- KUWAHARA K., NAKAE S. & YAO A. 1991. Late Permian 'Toishi-type' siliceous mudstone in the Mino-Tamba Belt. *Journal of the Geological Society of Japan* **97**, 1005–8 (in Japanese with English abstract).
- LEHMANN R. F., BERNASCONI S. M., BARBIERI A. & MCKENZIE J. A. 2002. Preservation of organic matter and alteration of its carbon and nitrogen isotope composition during simulated and in situ early sedimentary diagenesis. *Geochimica et Cosmochimica Acta* **66**, 3573–84.
- LOOY C. V., BRUGMAN W. A., DILCHER D. L. & VISSCHER H. 1999. The delayed resurgence of equatorial forests after the Permian-Triassic ecologic crisis. *Proceedings of the National Academy of Sciences of the United States of America* **96**, 13 857–62.
- MAGARITZ M., KRISHNAMURTHY R. V. & HOLSER W. T. 1992. Parallel trends in organic and inorganic carbon isotopes across the Permian/Triassic boundary. *American Journal of Science* **292**, 727–39.
- MATSUDA T. & ISOZAKI Y. 1991. Well-documented travel history of Mesozoic pelagic chert in Japan: From remote ocean to subduction zone. *Tectonics* **10**, 475–99.
- MÜLLER K. J. 1956. Triassic conodonts from Nevada. *Journal of Paleontology* **30**, 818–30.
- MUNDIL R., LUDWIG K. R., METCALFE I. & RENNE P. R. 2004. Age and timing of the Permian mass extinctions: U/Pb dating of closed-system zircons. *Science* **305**, 1760–3.
- MUSASHI M., ISOZAKI Y., KOIKE T. & KREULEN R. 2001. Stable carbon isotope signature in the mid-Panthalassa shallow-water carbonates across the Permian-Triassic boundary: Evidence for ^{13}C -depleted superocean. *Earth and Planetary Science Letters* **191**, 9–20.

- NAKAE S. 1993. The Permo-Triassic boundary as a decollement zone within pelagic siliceous sediments, with reference to Jurassic accretion of the Tamba Terrane, SW Japan. *Bulletin of the Geological Survey of Japan* **44**, 471–81 (in Japanese with English abstract).
- ODA H. & SUZUKI H. 2000. Paleomagnetism of Triassic and Jurassic red bedded chert of the Inuyama area, central Japan. *Journal of Geophysical Research* **105**, 743–67.
- OHKOUCHI N., NAKAJIMA Y., OKADA H. *et al.* 2005. Biogeochemical processes in the saline meromictic Lake Kaiike, Japan: Implications from molecular isotopic evidences of photosynthetic pigments. *Environmental Microbiology* **7**, 1009–16.
- ORCHARD M. J. 1995. Taxonomy and correlation of Lower Triassic (Spathian) segminate conodonts from Oman and revision of some species of Neospathodus. *Journal of Paleontology* **69**, 110–22.
- ORCHARD M. J. 2007. Conodont diversity and evolution through the latest Permian and Early Triassic upheavals. *Palaeogeography, Palaeoclimatology, Palaeoecology* **252**, 93–117.
- OVCHAROVA M., BUCHER H., SCHALTEGGER U., GALTETTI T., BRAYARD A. & GUÉX J. 2006. New Early to Middle Triassic U-Pb ages from South China: Calibration with ammonoid biochronozones and implications for the timing of the Triassic biotic recovery. *Earth and Planetary Science Letters* **243**, 463–75.
- PAYNE J. L., LEHRMANN D. J., WEI J., ORCHARD M. J., SCHRAG D. P. & KNOLL A. H. 2004. Large perturbations of the carbon cycle during recovery from the End-Permian extinction. *Science* **305**, 506–9.
- SCHUBERT J. K. & BOTTJER D. J. 1995. Aftermath of the Permian-Triassic mass extinction event: Paleocology of Lower Triassic carbonates in the western USA. *Palaeogeography, Palaeoclimatology, Palaeoecology* **116**, 1–39.
- SHIBUYA H. & SASAJIMA S. 1986. Paleomagnetism of red cherts: A case study in the Inuyama area, central Japan. *Journal of Geophysical Research* **91**, 105–16.
- SUGIYAMA K. 1992. Lower and middle Triassic radiolarians from Mt. Kinkazan, Gifu Prefecture, central Japan. *Transaction and Proceedings of the Palaeontological Society of Japan, New Serie* **167**, 1180–223 (in Japanese with English abstract).
- SUGIYAMA K. 1997. Triassic and Lower Jurassic radiolarian biostratigraphy in the siliceous claystone and bedded chert units of the southeastern Mino Terrane, Central Japan. *Bulletin of the Mizunami Fossil Museum* **24**, 79–193.
- TADA R., WATANABE S., KASHIYAMA Y. *et al.* 2005. High-resolution analysis of Late Paleozoic-Early Mesozoic variability of paleoceanographic system recorded in bedded chert sequence in the inner zone of southwest Japan. *Journal of Geography* **114**, 638–42 (in Japanese with English abstract).
- TAKAHASHI S., YAMAKITA S., SUZUKI N., KAIHO K. & EHIRO M. 2009a. High organic carbon content and a decrease in radiolarians at the end of the Permian in a newly discovered continuous pelagic section: A coincidence? *Palaeogeography, Palaeoclimatology, Palaeoecology* **271**, 1–12.
- TAKAHASHI S., OBA M., KAIHO K., YAMAKITA S. & SAKATA S. 2009b. Panthalassic oceanic anoxia at the end of the Early Triassic: A cause of delay in the recovery of life after the end-Permian mass extinction. *Palaeogeography, Palaeoclimatology, Palaeoecology* **274**, 185–95.
- WIGNALL P. B., BOND D. P. G., KUWAHARA K., KAKUWA Y., NEWTON R. J. & POULTON S. W. 2010. An 80 million year oceanic redox history from Permian to Jurassic pelagic sediments of the Mino-Tamba terrane, SW Japan, and the origin of four mass extinctions. *Global and Planetary Change* **71**, 109–23.
- YAMAKITA S. 1987. Stratigraphic relationship between Permian and Triassic strata of chert facies in the Chichibu terrane in eastern Shikoku. *Journal of the Geological Society of Japan* **93**, 145–8 (in Japanese with English abstract).
- YAMAKITA S. 1993. Conodonts from P/T boundary sections of pelagic sediments in Japan. *Abstract, The 100th Annual Meeting of the Geological Society of Japan*, pp. 64–5 (in Japanese).
- YAMAKITA S. & KADOTA N. 2001. Early Triassic conodonts from the upper part of the black carbonaceous claystone layer of the Tenjinmaru P/T boundary section in Northern Chichibu Belt, Southwest Japan. *Abstract, The 150th Regular Meeting of the Palaeontological Society of Japan*, p. 61 (in Japanese).
- YAMAKITA S., TAKAHASHI S. & KOJIMA S. 2010. Conodont-based age-determination of siliceous claystone in the lower part of the Momotaro-jinja section, Inuyama, central Japan. *Abstract, The 2010 Annual Meeting of the Palaeontological Society of Japan*, p. 47 (in Japanese).
- YAMAKITA S., KADOTA N., KATO T. *et al.* 1999. Confirmation of the Permian/Triassic boundary in deep-sea sedimentary rocks: Earliest Triassic conodonts from black carbonaceous claystone of the Ubara section in the Tamba Belt, Southwest Japan. *Journal of the Geological Society of Japan* **105**, 895–8.
- YAO A. 1982. Middle Triassic to Early Jurassic radiolarians from the Inuyama area, central Japan. *Journal of Geosciences, Osaka City University* **25**, 53–70.
- YAO A. & KUWAHARA K. 1997. Radiolarian faunal change from Late Permian to Middle Triassic times. *News of Osaka Micropalaeontologists, Special Volume* **10**, 87–96 (in Japanese with English abstract).
- YAO A., MATSUDA T. & ISOZAKI Y. 1980. Triassic and Jurassic radiolarians from the Inuyama area, central Japan. *Journal of Geosciences, Osaka City University* **23**, 135–54.
- YIN H., FENG Q., LAI X., BAUD A. & TONG J. 2007. The protracted Permian-Triassic crisis and multi-episode extinction around the Permian-Triassic boundary. *Global and Planetary Change* **55**, 1–20.